2010-07-13

Prediction and Study of Binary Alloys Using First-Principles Methods

Richard Hansen Taylor II
Brigham Young University - Provo

BYU ScholarsArchive Citation

Taylor, Richard Hansen II, "Prediction and Study of Binary Alloys Using First-Principles Methods" (2010). *All Theses and Dissertations*. 2564.
https://scholarsarchive.byu.edu/etd/2564

PREDICTION AND STUDY OF BINARY ALLOYS USING FIRST-PRINCIPLES METHODS

by

Richard H. Taylor

A thesis submitted to the faculty of
Brigham Young University
in partial fulfillment of the requirements for the degree of

Master of Science

Department of Physics and Astronomy
Brigham Young University
August 2010

BRIGHAM YOUNG UNIVERSITY

GRADUATE COMMITTEE APPROVAL

of a thesis submitted by

Richard H. Taylor

This thesis has been read by each member of the following graduate committee and by majority vote has been found to be satisfactory.

Date	Gus L. W. Hart, Chair
Date	Harold T. Stokes
Date	Bret C. Hess

BRIGHAM YOUNG UNIVERSITY

As chair of the candidate's graduate committee, I have read the thesis of Richard H. Taylor in its final form and have found that (1) its format, citations, and bibliographical style are consistent and acceptable and fulfill university and department style requirements; (2) its illustrative materials including figures, tables, and charts are in place; and (3) the final manuscript is satisfactory to the graduate committee and is ready for submission to the university library.

Date	Gus L. W. Hart Chair, Graduate Committee

Accepted for the Department

J. Ward Moody, Graduate Coordinator
Department of Physics and Astronomy

Accepted for the College

Thomas W. Sederberg, Associate Dean
College of Physical and Mathematical Sciences

ABSTRACT

PREDICTION AND STUDY OF BINARY ALLOYS USING FIRST-PRINCIPLES METHODS

Richard H. Taylor

Department of Physics and Astronomy

Master of Science

The utility of first-principles methods in the study and prediction of binary alloys is showcased by three detailed studies. In particular, the $T = 0\,\mathrm{K}$ cluster expansion methodology in conjunction with finite temperature statistical modeling by a Monte Carlo method is used to study two systems of practical interest, Mg-Li (magnesium-lithium) and Rh-W (rhodium-tungsten). Also, an empirically-informed, high-throughput approach to crystal structure prediction is shown by a study of the $\mathrm{Pt_8Ti}$ (the Pietrokowsky phase) phase and a broad and detailed analysis of binary Mg-X phases in 39 systems (X=Ag, Al, Au, Ca, Cd, Cu, Fe, Ga, Ge, Hf, Hg, In, Ir, K, La, Li, Pb, Pd, Pt, Mo, Na, Nb, Os, Rb, Re, Rh, Ru, Sc, Si, Sn, Sr, Ta, Tc, Ti, V, W, Y, Zn, Zr). These results are presented in the form of three publications (the first two are in print, and the third is nearing submission) co-authored with Gus Hart and Stefano Curtarolo.

ACKNOWLEDGMENTS

I would like to thank the faculty of the BYU Physics and Astronomy Department, whose help and encouragement have made the completion of this degree possible.

Contents

List of Figures

Chapter 1

Ordered magnesium-lithium alloys: First-principles predictions

1.1 Motivation and Background

Emerging technologies increasingly depend on the production of ultra-lightweight materials. Magnesium-lithium (Mg-Li) alloys are the lightest metallic alloys, having densities near that of plastics [1–3], and are strong enough to be used in a variety of high-performance applications. In particular, Mg-Li alloys are good candidates for material applications in industries such as aerospace and automotive manufacturing [4].

As an alloying agent in magnesium, lithium is advantageous principally because of its low density and cubic crystal structure. The addition of lithium converts the hexagonal close packed (hcp) structure of natural magnesium to a more ductile and formable body centered cubic (bcc) alloy. Addition of 13 atomic % Li partially converts the alloy to a cubic structure and content exceeding 33 atomic % results in total conversion [5].

Although the Mg-Li system has been studied extensively [5–11], evidence suggesting the formation of ordered phases is notably sparse. Diffusionless transformations of the martensitic type have been observed in pure Li, and similar transformations occur in low temperature magnesium alloyed lithium at certain concentrations [11, 12]. Binary ordered-phases have not been conclusively identified, however, and any instances contained in the literature are indeterminate [6, 9, 13, 14].

The results of high-throughput (HT) *ab initio* calculations performed with the AFLOW package (described later) show, however, that the heat of formation is negative for a large number of potential structure types, implying the existence of at least one thermodynamically stable ordered phase (Figure1.1).

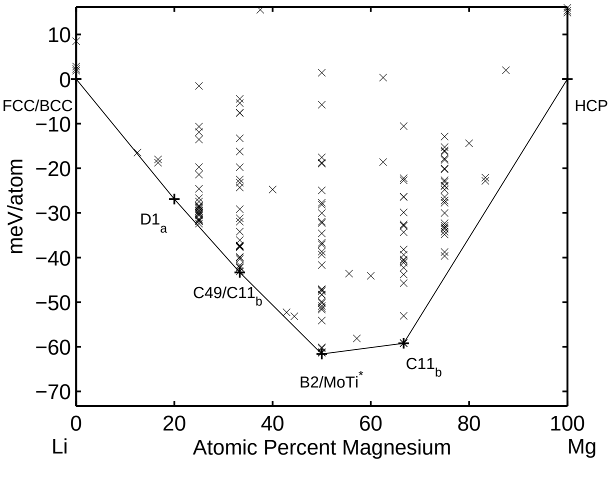

Figure 1.1 High-throughput formation enthalpy calculations for Mg-Li. Structures resting on the convex hull are labeled according to their Strukturbericht designation and are displayed prominently. Note that many computed structures have negative formation enthalpy, suggesting an ordering system. MoTi* prototype from Ref. [15].

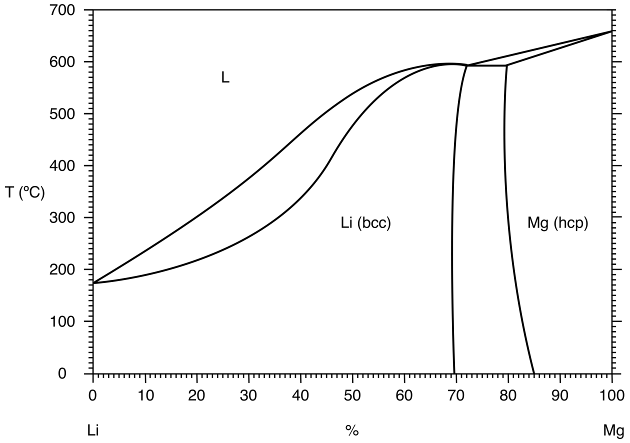

Figure 1.2 Schematic LiMg phase diagram constructed after Ref. [8,16–20]

1.2 First principles method

Following the HT results, we have made predictions of Mg-Li ordered phases using the *cluster expansion method*—a first-principles based approach in which input data is mapped to a truncated Ising-like Hamiltonian. The configurational Hamiltonian allows for a fast ground state search (GSS) over many derivative superstructures [1]. The cluster expansion (CE) method was applied to the Mg and Li lattice configurations (bcc and hcp respectively). Although minimum energy configurations may exist outside those considered, superstructures derived from the parent lattices of the alloy constituents generally include the lowest energy configurations. This assumption is particularly supported for Mg-Li by the existence of bcc derivative superstructures exclusively as ground states in the HT results and by phases present in experimental phase diagrams (Fig. 1.2).

---

[1] The GSS results presented here were performed over 16,098 bcc and 15,975 hcp derived superstructures. Searches including many more structures were also performed but yielded no new ground states.

Quantum mechanical energies used for the HT and CE approaches were computed using density functional theory as implemented by the Vienna *ab initio* Simulation Package software [21]. Following the method of Froyen [22], so-called "equivalent points" were used to form the **k**-point mesh, resulting in reduced systematic error in the calculation of formation enthalpy. Perdew-Burke-Ernzerhof (PBE) projector augmented wave (PAW) pseudopotentials with semi core s and p states treated as valence were used [23, 24]. The plain wave energy cutoff was approximately 339 eV. Energies were calculated at zero temperature and pressure without spin polarization, zero-point motion or lattice vibrations. All crystal structures were fully relaxed (cell volume and shape and the basis atom coordinates inside the cell). Numerical convergence to about 1 meV/atom was ensured by the high energy cutoff and by dense **k**-point meshes.

In the HT work, the calculations were performed using the high-throughput framework AFLOW [15, 25–28]. For each system, the energies of 204 crystal structures were calculated. In addition to the 176 configurations described in [15], these included all the symmetrically-distinct hcp-, bcc-, fcc-based superstructures [29,30] with up to four atoms per cell, and additional prototypes [2]. The additional prototypes were considered because they are common or related to Mg alloys [32,33]. This protocol gives reasonable results. In Ref. [15], it was shown that the probability of reproducing the correct ground-state, if well defined and not ambiguous, is $\eta_c^\star \sim 96.7\%$ (*"reliability of the method"*, Eq. (3)). For the HT approach, we did not consider lattice-superstructures

---

[2] A5, A6, A7, A8, A9, A11, B20, C36, D5$_{19}$, Al_2Zr_4, Al_3Zr_2, CdTi, $CuPt_7$, Cu_3Ti_2, Ga_2Hf, Ga_4Ni, Ga_3Pt_5, Ga_4Ti_5, Hg_2Pt, ITl, InTh, LiB-MS1/2 [31], $NbNi_8$, $NiTi_2$ SeTl, and V_4Zn_5

with more than four atoms per cell due to the fact that their number increases exponentially[3]. Therefore, even if it is impossible to rule out the existence of an undetected ground-state, the protocol is expected to give a reasonable balance between high-throughput speed and scientific accuracy to determine miscibility of Mg-Li alloys.

1.3 Cluster Expansion Method and Ground State Search results

In the CE formalism, atomic configuration is defined by first associating a set of ‘spin’ values to atomic type. The configurational properties of a structure are then captured by the averages of spin products or values of *correlation functions* on the lattice.

The correlation functions, evaluated over each symmetrically unique ‘cluster,’ form a mathematically complete basis for a lattice of size N by which any configurational property may be expanded [35]. A set of constants termed *effective cluster interactions* (ECIs) form the coefficients of the expansion by which the material property in question is expressed.

The utility of the CE method is that a physical quantity such as energy may be expanded entirely in configuration space. This allows for exhaustive searches over configurational domains in order for example to find minima. Given cluster expanded formation enthalpy, minimum energy structures serve as strong candidates for thermodynamically stable ordered states. In the

---

[3] It should also be noted that systems exist which do not conserve the parents’ lattice (i.e. Hf-Ti, Hf-Zr [34]).

case of a binary system, the CE expresses the energy of a lattice configuration σ as

$$\mathrm{E}_{\mathrm{CE}}(\sigma) = J_0 + \sum_f \sum_1^{N_f} \Pi_f(\sigma) J_f, \tag{1.1}$$

where σ defines the occupation of N lattice sites by A and B atoms, J_f is the ECI for cluster f, N_f is the number of clusters of type f, and Π_f are the averaged spin (± 1 for binary systems) products for cluster f in configuration σ.

Effective cluster interactions were found using least-squares regression and a genetic algorithm [36, 37]. The method we employed involved two general steps as implemented in the Universal Cluster Expansion software package [38]. (Alternatively, the packages CLUPAN and ATAT could be used to the same effect. See for example, [39–41]). First, a set of figures (*correlation functions*) was selected from a large pool generated from the parent lattice. The set of figures is typically smaller than the input data set and may be no larger if the system is to be well defined. Second, least-squares regression was used to determine the ECIs corresponding to these figures, given the input data. In short, the figure pool comprised the sample-space from which many candidate fits were generated.

The fits were then scored using *leave one out cross validation* (LOOCV). Given n input structures, LOOCV provides a quantitative measure of the quality of fit by averaging the error found using $n - 1$ structures (training data) to predict 1 structure (validation data) for each of the n structures:

$$\mathrm{S}_{\mathrm{cv}} = \frac{1}{n} \sum_{i=1}^{n} |\mathrm{E}_{\mathrm{CE}}(\sigma_n) - \mathrm{E}_{\mathrm{DFT}}(\sigma_n)| \tag{1.2}$$

The cross validation score (CVS), in units of energy, should be a small fraction of the energies of input structures so that reliable results are obtained.

Typical fitting errors for the Mg-Li system were between 0 and 3 meV/atom. With input energies near -30 meV/atom, the errors were in the reasonable range. A total of 83 and 73 structures comprised the input data set used in the construction of bcc and hcp CEs respectively.

Once a CE was constructed, a *ground state search* was performed over large numbers of derivative superstructures (see Fig. 1.3). Thermodynamically stable ground states, however, are not necessarily the minimum energy configurations at each concentration. One usually encounters a concentration in which the average energy of two structures with neighboring concentrations yield a mixed phase with lower total energy. The *tie lines* connecting all pairs of minimum energy structures were thus determined. When the structure in question rests below all such tie lines it was included as a ground state. The complete set of structures determined in this manner comprise the minimal convex set of structures (the convex hull). Fig. 1.3 includes the convex hulls for the bcc and hcp Mg-Li CE constructed using the predicted energies from fits generated using 83 and 73 input structures respectively.

The *absolute minima* within the set of configurations that included both bcc and hcp superstructures were found by scaling hcp structure formation enthalpy by the difference in free energy of pure Mg and Li according to concentration. The free energy was computed for hcp Mg and Li and bcc Mg and Li, and the formation enthalpy of hcp structures were adjusted in the following manner:

$$H \rightarrow H + (x\Delta H_{\mathrm{Mg}} + (1-x)\Delta H_{\mathrm{Li}}), \tag{1.3}$$

Here H is the formation enthalpy of a ground state structure, x is the concentration of Mg, and ΔH_{Mg} and ΔH_{Li} are the differences in the hcp and bcc free energies of Mg and Li. CE predicted energies shown in Fig. 1.3 scaled relative

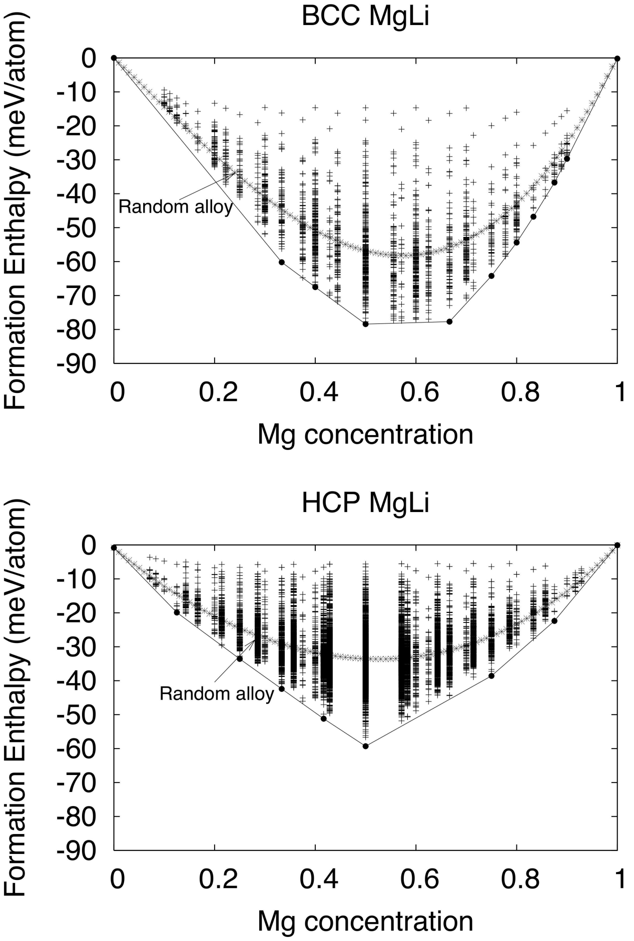

Figure 1.3 Formation enthalpy versus concentration for many derivative superstructures. The random alloy energy is included as well as the convex hull. Points on the convex hull indicate thermodynamically stable ground state structures

to one another in this fashion are shown in Fig. 1.4.

In the case of bcc Mg-Li, the convex hull constructed using DFT energies of CE predicted ground states reveal ground states $C11_b$, B2, and $L6_0$ (see the Appendix for details of the method used). These structure types are in agreement with the HT results and are referred to by their *Strukturbericht* designation. It is perhaps of interest to note that the ground state structures are several meV lower than the structure nearest in energy with the same concentration except at 50% (B2). In the case of B2, the energy is found

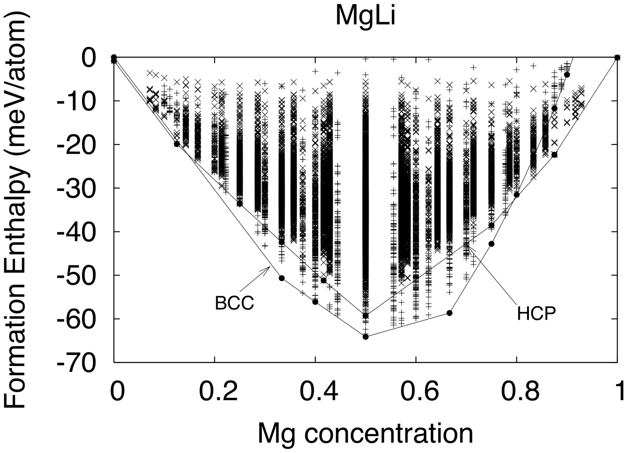

Figure 1.4 CE formation enthalpies as a function of concentration. Energy predictions from the hcp CE are shifted according to the difference in free energy of Mg and Li on bcc and hcp lattices. Note the two-phase region of bcc and hcp phases on the Mg rich side consistent with known phase data (Fig. 1.2)

to be only slightly lower than an A_2B_2 structure with [011] directed stacking planes (similar to the NbP face-centered-cubic superstructure) (Fig. 1.5). A slight difference in formation enthalpy is evidently the reason many CEs were unable to accurately predict the relative energies of this NbP-like structure (corresponding to structure 19 in Table 1) and the true ground state, B2.

Mg-Li ground state predictions on the hcp lattice were treated in the same manner as the bcc structures, i.e., VASP was used to directly compute their energies from which the ground states were determined. Ground states were found at concentrations $x = 1/8$, $1/2$, $2/3$, and $3/4$ Mg. In this case, the configurations do not correspond to known structures. Hcp phases were higher in energy than the bcc ground states across the concentration range excluding pure Mg (see figure 1.6). From the superposed energies of bcc and hcp Mg-Li, it can be seen that the two-phase region that extends from from approximately 17 atomic % Li at finite temperatures broadens as the temperature is lowered

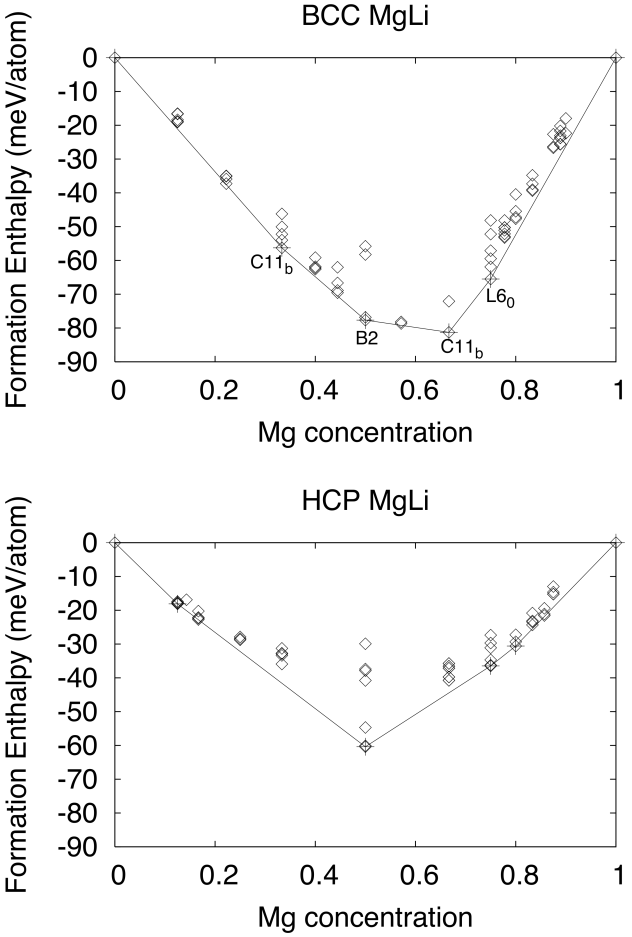

Figure 1.5 Final ground state predictions for bcc and hcp Mg-Li using energies computed with VASP. The tie lines are shown. The hcp ground states do not correspond to commonly known structure types.

and the solubility of Mg in Li decreases.

1.4 Order-disorder transitions predicted by Monte Carlo simulation

Complex Ising-like Hamiltonians with many couplings are notoriously difficult to extend to finite temperatures with Monte Carlo (MC) methods, especially

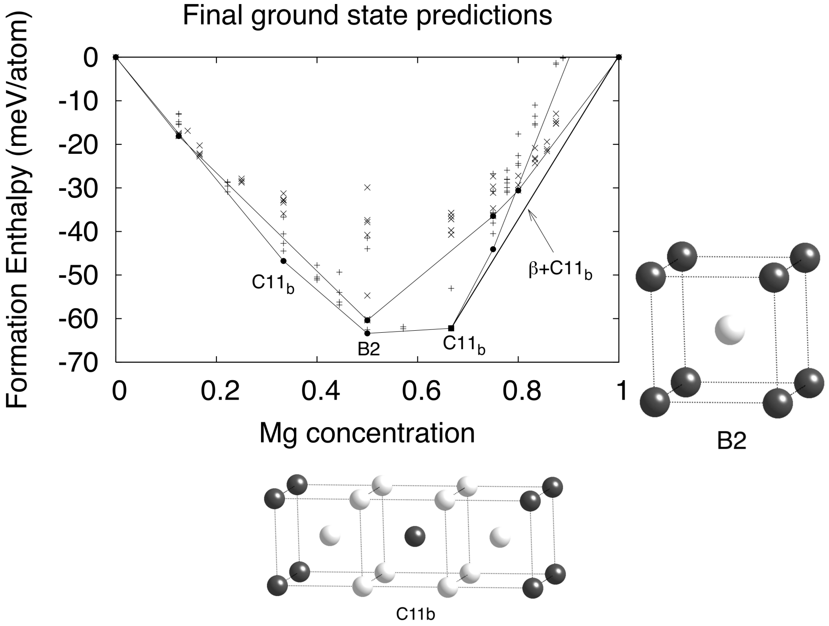

Figure 1.6 Final ground state predictions for hcp and bcc Mg-Li. The hcp energies are shifted relative to bcc energies. Note that there is no hcp phase predicted other than pure Mg and the two-phase region extending to 2/3 Mg. The structures B2 and C11b are also shown from left to right.

in the low temperature region [42]. Numerical problems also arise when one attempts to model the system around the critical temperature (i.e., due to critical slowing). In general, the behavior of systems containing many interactions is not well understood, and MC convergence times often make the task of modeling the system nearly intractable.

The CEs we constructed for Mg-Li utilized large numbers of figures in order to provide accurate energy predictions across the concentration range. As a result, however, Monte Carlo simulations involving these complex Hamiltonians present significant numerical difficulties. If determining the critical temperature is to be computationally feasible, it is necessary to simplify the complex CE to one that involves fewer interactions.

Although the simplified CE is certainly incapable of predicting the behavior of ordering as accurately as one containing many figures, by ensuring the proper ground states and energies are predicted, sufficiently accurate conclusions may be made. Further, rather than a detailed study of the nature of the transition, it was our primary interest to determine *generally* where the order-disorder transitions occur in order to guide experimental attempts to realize the ordered phases.

For the above reasons, a 5-term CE on the bcc lattice was constructed for the purposes of conducting finite temperature MC simulations. The statistical analysis conducted on many CEs provided the criteria by which we were able to narrow the selection of between many 5-term CEs. Specifically it was required that the 5-term CE predicted ground states at 1/3 1/2 and 2/3 magnesium with structure types, C11$_b$, B2, and C11$_b$, respectively, and that predicted energies were comparable to those computed using first-principles methods. In the 5-term CE, predicted energies differed from DFT calculations on average less than 5meV (roughly an order of magnitude smaller than input energies).

Canonical Monte Carlo simulations were performed using the 5-term CE on a $30 \times 30 \times 30$ bcc lattice with periodic boundary conditions. Equilibration times were between 5×10^6 and 15×10^6 MC steps. The temperature was decreased uniformly in decrements of 10 K initially from 2000 K to 50 K. Transitions were identified by calculating the specific heat, using the usual statistical relation involving the mean square deviation of the energy from the mean value [42],

$$\sigma_E^2 = < \mathrm{E}^2 > - < \mathrm{E} >^2 = \frac{\mathrm{C}}{k\beta^2}. \tag{1.4}$$

Fig. 1.7 displays the configurational specific heat of the three predicted ordered phases.

Transition temperatures were estimated by identifying the ‘divergence’ in the heat capacity; the structure types $C11_b$ exhibit transitions at approximately 190 K and 210 K for 1/3 and 2/3 Mg respectively. Simulations at 50 %, B2, exhibited more resistance to equilibration and required many more flips per MC time. Nevertheless, the transition was identified to be between 300 and 450 K by pair correlation values. Comparison of pair correlation values of the MC cell with the CE predicted ground state structures reveals good agreement after the transition. At 50 % the correlation values approach those of the expected B2 structure gradually over the temperature region shown (Fig. 1.7), suggesting that although the system was not fully equilibrated an order-disorder transition had occurred.

The range of transition temperatures predicted by the MC simulations is generally supported by the results of sonic measurements for low temperature Mg-Li alloys: In the work of Barrett and Trautz [12], the onset of spontaneous structural transitions were measured by recording audible clicks, the result of the rapid shearing motions that accompany the transition. For materials containing a large percentage of Mg content, few audible clicks were heard, and the specific nature of the partial ordering was not identifiable by diffraction techniques. However, the *onset* of spontaneous ordering for alloys containing greater than 20 atomic % Mg were determined by noting the temperature at which the first clicks were heard and was estimated between 140K and 200K.

1.5 Conclusion

In conclusion, the CE method predicts bcc ordered phases at several concentrations including one which may be well suited for structural applications,

$C11_b$. With the exception of pure Mg, hcp phases were found to be higher in energy than bcc ground states across the concentration range. Order-disorder transition temperatures, predicted by MC simulations, have been reported for the three bcc ordered structures between 200 and 400K.

The predicted low temperature transitions of the Mg-Li bcc ordered phases possibly explain why they have evaded experimental observation despite a relatively large amount of investigation in the system. Additionally, developing methods to experimentally realize the Mg-Li ordered phases is likely to require significant effort due in particular to the low temperatures of the transitions and possible kinetic limitations.

However, the bulk low temperature phases should not be ruled out, even at high-temperature. Size-induced stabilization present at the nanoscale [43, 44] may promote stability at higher temperature for nano-dispersed precipitates. Although the mechanical properties would not modify the solid-solution Mg-Li appreciably, the overall effect in thermal and electric transport can be dramatic, as it has been shown for nano-precipitates in semiconducting materials [45–47]. Thus, the enhanced structural properties of alloys containing even small amounts of ordering provide a significant incentive in this regard. Furthermore, low temperature ordering has the inherent advantage of increased stability at higher temperatures possibly allowing for practical application of the ordered alloys if initially realized.

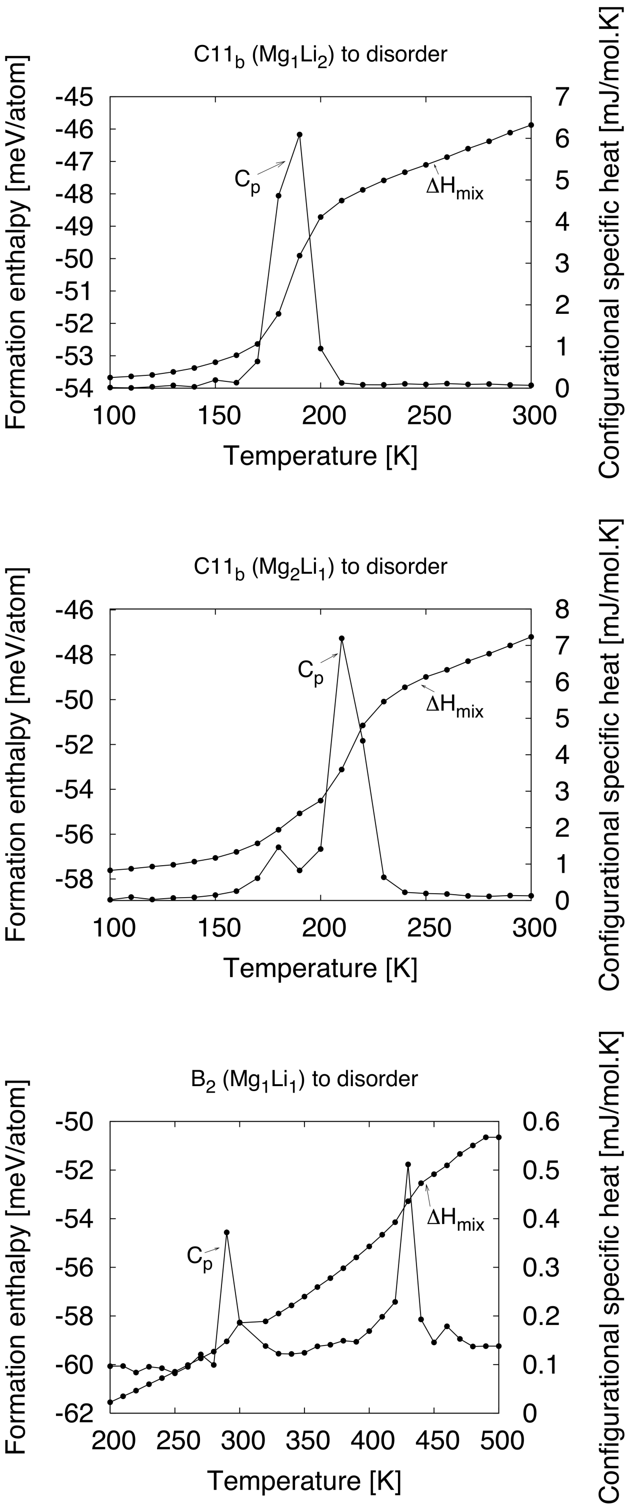

Figure 1.7 Specific heat C$_p$ of Mg-Li ordered phases with temperature increased in increments of 10K. Formation enthalpy is overlaid including the scale indicated on the left.

Chapter 2

Predictions of the Pt_8Ti phase in unexpected systems

2.1 Introduction

Binary ordered phases with high stoichiometric ratio compositions (7:1 and higher) are rare [32, 33]. Despite the rarity of phases with stoichiometry far from 1:1, however, there is considerable interest in identifying their existence. Beyond the fundamental scientific motivation to characterize the complete ground states of binary systems, it is well known that even small amounts of an alloying agent may result in dramatic material enhancements when ordering occurs (e.g., strength [48, 49]). To illustrate this point, consider the case of order-induced hardening in platinum-copper (Pt-Cu) [50]. The addition of 14 at. % Cu in Pt can result in the formation of ordered domains of the type A_7B [51], increasing the hardness in some instances by more than double that of untreated specimens.

Of the few high-stoichiometry phases, the A_8B phase (Pearson symbol tI18 and Space Group *I4/mmm* [52]) is of particular interest—it forms in systems containing elements from the transition metal group and has potential applications in catalysis, high-temperature electrodes, and jewelry. It was first reported by Pietrokowsky in 1965 in Pt-Ti (hence prototype Pt_8Ti [53]) [54] and has since been found in 11 metallic systems. In order of discovery they are Pt_8Ti [54], Pt_8Zr [55], Ni_8Nb [56], Ni_8Ta [57], Ni_8V [58], Pd_8W [59], Pd_8V [60], Pt_8V [52], Ni_8Mo [61], Pd_8Mo [62], and Pt_8Cr [63].

Systems found to exhibit the A_8B phase are limited to combinations of the transition metals—specifically to group 10 alloyed with group 4–6 (IUPAC nomenclature) elements—indicating a correlation between the localized unfilled *d*-orbitals and formation of the 8:1 phase. Further, one notes that the elemental phase of the concentration rich element is face centered cubic (fcc) in every case, as expected because A_8B is a fcc derivative superstructure.

With these general observations in mind, it was natural to explore the group 9 fcc elements, Rh and Ir, alloyed with group 4–6 elements, as candidate systems. Experimental and theoretical [64] investigation of A_8B has largely been limited to group 10 elements as the concentration rich constituent, perhaps due to their similarity to platinum and implications of the Pettifor-type structure map [65].

A structure map of the Pettifor type is shown in Fig. 2.2(a). Known A_8B phases and likely stable phases are indicated in the diagram and summarized by Ardell [60]. When the candidates are compared with the results of *high-throughput* calculations (see Methods section), however, several phases (Rh-W, Rh-Mo, Ir-W, Pt-Hf) not included in the Pettifor map are predicted thermodynamically stable (Fig. 2.2). Scandium phases (Pd_8Sc and Pt_8Sc) were also found (although not shown in the figure), the existence of which is indeed

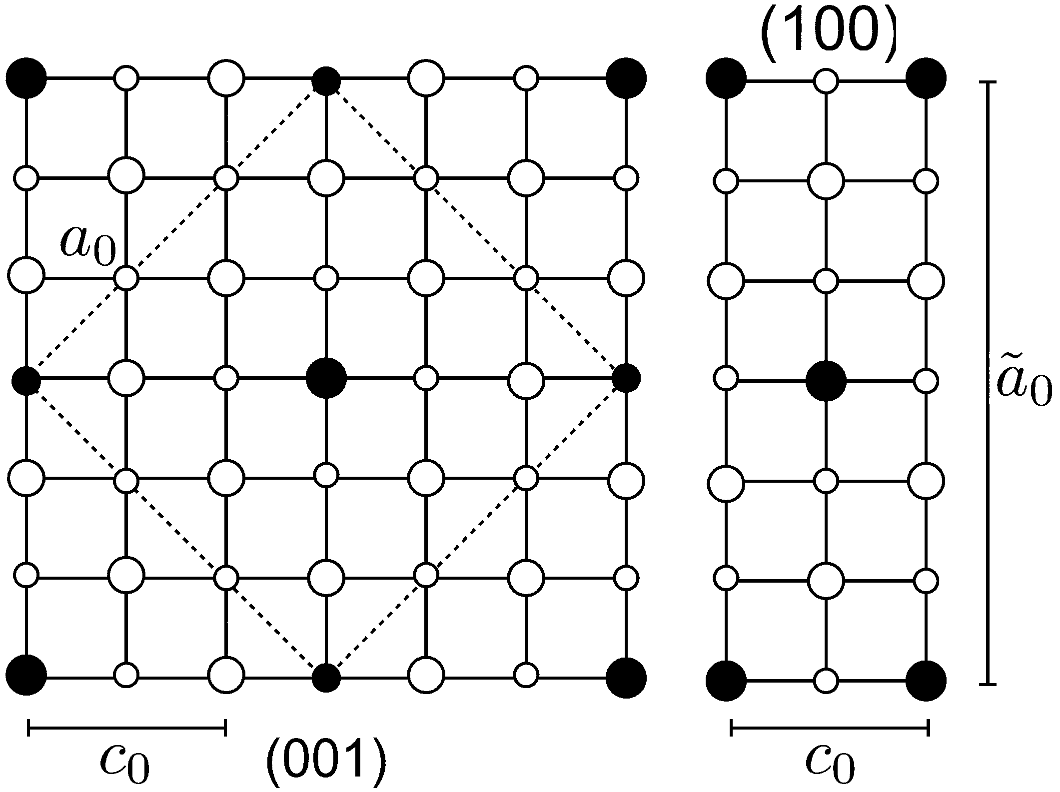

Figure 2.1 Projections of the A_8B phase along (001) and (100). Atoms sit on fcc lattice sites, with large circles indicating atoms in the plane of the pages and small circles suggesting a displacement $a/2$ perpendicular to the plane. The bct unit cell is indicated by the dashed lines. A non-primitive face centered tetragonal cell is outlined by the perimeter.

surprising in this light, as the Mendeleev number of Sc is smaller than all the rare earths, none of which have been shown to form the A_8B phase.

2.2 Methods

In the HT approach, previously unexpected ground states are found by a brute force search— formation enthalpies are calculated for essentially every crystal structure ever observed in binary metal systems as well as a large number of enumerated derivative superstructures [67]. For this study, the calculations

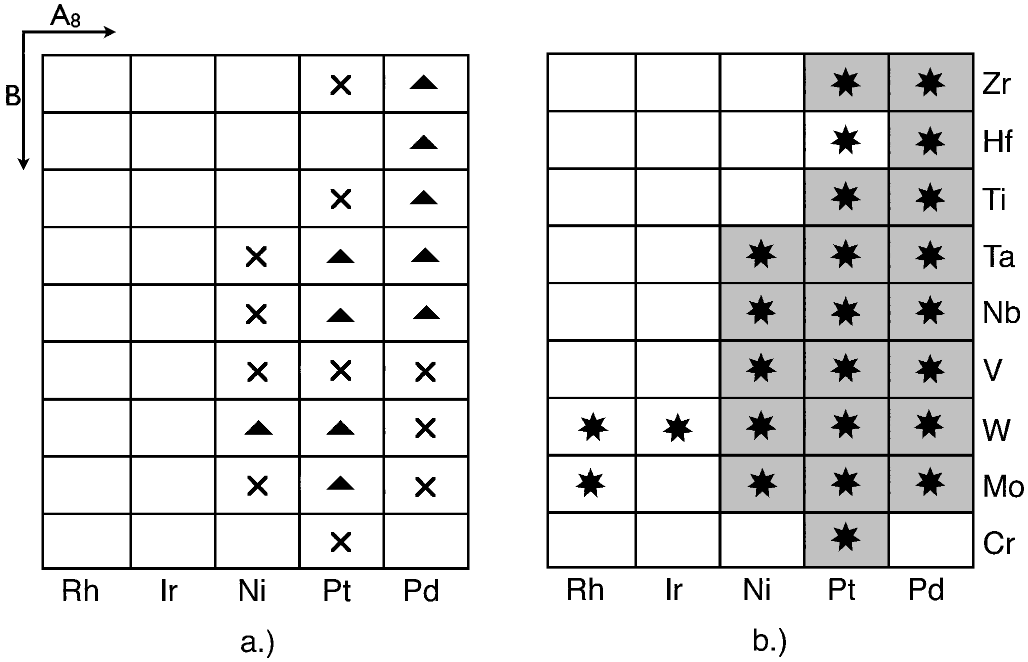

Figure 2.2 a.) A Pettifor-type structure map of the A_8B phase in the Rh, Ir, Ni, Pt and Pd systems. The concentration-rich elements are listed horizontally. Both axes are labeled by increasing Mendeleev number. Predictions given by Ardell [66] are labeled with a triangle and experimentally observed systems are labeled with a cross. b.) HT predictions are indicated by a star. Overlap with experiment and predictions is complete (indicated by the shaded region). Our predictions, however, are not limited to these results (e.g., Rh-W).

were performed using the AFLOW framework [25,28,34,68,69] based on *ab initio* calculations of the energies by the VASP software [70]. We used projector augmented waves (PAW) pseudopotentials [23] and the exchange-correlation functionals parameterized by Perdew, Burke and Ernzerhof [71] for the generalized gradient approximation (GGA). The energies were calculated at zero temperature and pressure (thus energies and enthalpies coincide), with spin polarization and without zero-point motion or lattice vibrations (zero-point motion is negligible because we do not consider light elements). All crystal structures were fully relaxed (cell volume and shape, and atomic positions). Numerical convergence to about ~ 1 meV/atom was ensured by a high energy cutoff (30% higher than the highest energy cutoff for the pseudopotentials of the components) and dense 6000 **k**-point Monkhorst-Pack meshes.

The high-throughput search included the 435 binary intermetallics that can be made with transition metals (La included). For each system, the energies of 200 crystal structures were calculated. In addition to the 176 configurations described in [68], these included all the symmetrically-distinct hcp-, bcc-, fcc-based superstructures [67] with up to four atoms per cell, and the prototypes A5, A6, A7, A8, A9, A11, B20, C36, $D5_{19}$, Al_2Zr_4, Al_3Zr_2, CdTi, $CuPt_7$, Cu_3Ti_2, Ga_2Hf, Ga_4Ni, Ga_3Pt_5, Ga_4Ti_5, Hg_2Pt, ITl, InTh, LiB-MS1/2 [31, 72], $NbNi_8(Pt_8Ti)$, $NiTi_2$, SeTl and V_4Zn_5. The additional prototypes were considered because they are common or related to noble metal alloys [32, 33]. We did not consider lattice-superstructures with more than four atoms per cell due to the fact that their number increases enormously It should also be noted that systems exist which do not conserve the parents' lattice (i.e. Hf-Ti, Hf-Zr [34]).

This procedure gives reasonable results as shown in Ref. [68]. Here it was shown that the probability of reproducing the correct ground-state, if well defined, not ambiguous, and present in our list of prototypes is $\eta_c^\star \sim 96.7\%$ (*"reliability of the method"*, Eq. (3) of Ref. [68]). There is no guarantee that the true ground states of a system will be found among the common experimentally observed structures or among small-unit-cell derivative structures. However, even if it is impossible to rule out the existence of an unexpected ground-state, this procedure (searching many enumerated derivative structures and exhaustively exploring experimentally reported structures) is expected to give a reasonable balance between high-throughput speed and scientific accuracy to determine the presence of A_8B phases.

2.3 Results and Discussion

Following the unexpected HT predictions shown in Fig. 2.2(b), the search for systems exhibiting A_8B was extended to all transition metals including lanthanum. The results of the HT search indicate thermodynamically stable and metastable (described below) A_8B phases in 59 systems. The phases are here listed: $Au_8Zn^\dagger$, $Cd_8Sc^\dagger$, $Cu_8Ni^\dagger$, $Cu_8Zn^\dagger$, Hg_8La, $Ir_8Os^\dagger$, Ir_8Re, $Ir_8Ru^\dagger$, Ir_8Tc, $Ir_8W^\dagger$, $Nb_8Os^\dagger$, $Nb_8Rh^\dagger$, $Nb_8Ru^\dagger$, $Nb_8Ta^\dagger$, Ni_8Fe, $Ni_8Mo^{\dagger\star}$, $Ni_8Nb^{\dagger\star}$, $Ni_8Ta^\star$, $Ni_8V^\star$, Ni_8W, $Pd_8Al^\dagger$, Pd_8Fe, Pd_8Hf, Pd_8Mn, $Pd_8Mo^\star$, Pd_8Nb, Pd_8Sc, Pd_8Ta, Pd_8Ti, $Pd_8V^\star$, $Pd_8W^\star$, Pd_8Zn, Pd_8Zr, $Pt_8Al^\dagger$, $Pt_8Cr^\star$, Pt_8Hf, Pt_8Mn, Pt_8Mo, Pt_8Nb, $Pt_8Rh^\dagger$, Pt_8Sc, Pt_8Ta, $Pt_8Ti^\star$, $Pt_8V^\star$, Pt_8W, $Pt_8Zr^\star$, Rh_8Mo, Rh_8W, Ta_8Pd, Ta_8Pt, Ta_8Rh, $V_8Cr^\dagger$, $V_8Fe^\dagger$, $V_8Ir^\dagger$, $V_8Ni^\dagger$, V_8Pd, V_8Pt, V_8Rh, $V_8Ru^\dagger$ (†=metastable, *=experimentally observed) (see fig 2.3). Thus, previously unsuspected occurrences of the A_8B phase are predicted in 36 systems. Some of the components in the predicted systems come from unexpected places on the periodic table (e.g., Hg-La) compared to the components in the experimentally known 8:1 phases.

Systems in which the A_8B structure is less than 3 meV above or below the tieline defined by adjacent ground states are labeled metastable (indicated by the blue tiles in Fig. 2.3). A definitive statement regarding the existence of a $T = 0\,\mathrm{K}$ ground state at 8:1 stoichiometry is difficult to make in these instances. Energies on the order of several meV are small in comparison with formation enthalpies of stable states in the systems studied and such small flucations may be due to systematic error in DFT calculations. Regardless of these considerations, however, metastable states are often realizable at finite temperature because of entropic stabilazation. Indeed, certain *experimental phases* (e.g., Ni_8Mo) are found to be *metastable* by our quantum mechanical calculations.

The case of Pt_7Cu was introduced at the beginning as an example of material improvement gained by ordering. More noteworthy, however, is the fact that a well-studied system yielded a previously unobserved ordered phase. Pt-Cu is a common jewelry alloy that has been investigated for decades and has been used for more than a century. Despite this, the ordered phase was only observed recently, after the appropriate sequence of annealing and cold working. Thus, one should not discount predicted phases merely because a system is well studied (e.g., Cu-Zn, Cu-Ni). Phases with finite order-disorder transitions may go unnoticed for many reasons, not the least of which is the real limitation imposed by kinetics. Several observed A_8B phases (Pd_8W, Pd_8V, and Pd_8Mo), for example, have only been realized after the introduction of excess vacancies by charged-particle irradiation [60].

Even so, since all HT quantum mechanical energy calculations were performed at zero temperature, it is possible that some of the predicted A_8B phases will not be observed experimentally. That is, it may be difficult to achieve thermal equilibriumin certain systems. The kinetics will be too slow to observe ordering in reasonable time if the concentration of thermally induced vacancies is too low.

To address this, it is desirable to leverage the synergy of an approach that combines [34] HT with a model that can be extended to finite temperature such as the cluster expansion (CE). Transition temperatures estimated by CE-

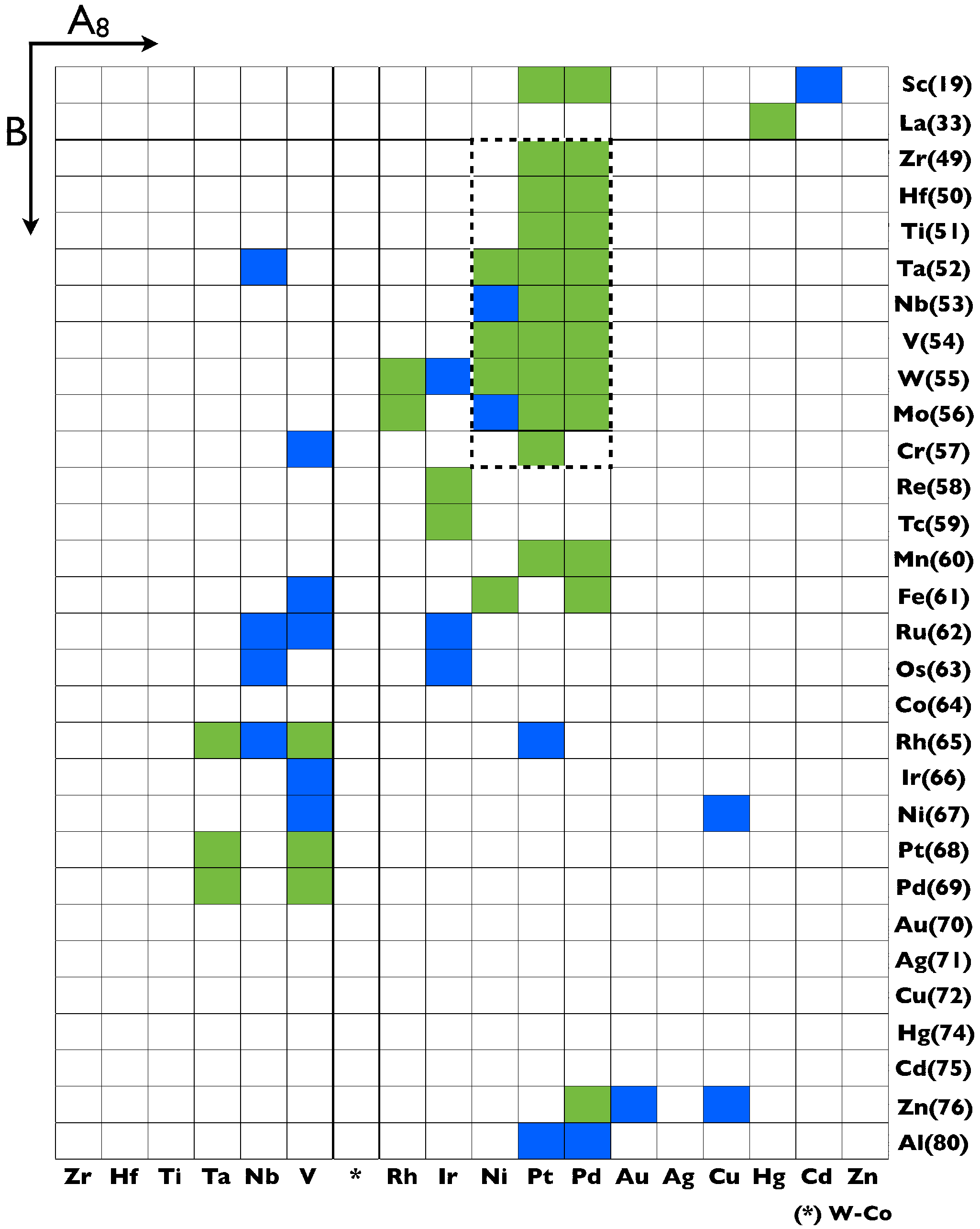

Figure 2.3 The complete set of A_8B phases predicted by HT calculations. Elements are listed according to the Mendeleev number after Pettifor [65]. Many previously unsuspected candidate systems are revealed, spanning the transition metals and La and Sc. 'W–Co' = W, Mo, Cr, Re, Tc, Mn, Fe, Ru, Os, and Co; No ground states at composition A_8B were found in this region.

based Monte Carlo simulations give an estimate of the likelihood of observing a transition experimentally.

We conducted a CE study, using the UNCLE [37, 38] code, on the A_8B forming Rh-W system. The CE was constructed using the energies of structures with concentrations in the range 0–25 at. % W (Fig. 2.4). At higher W concentration, HT results indicate that zero temperature ground states will not form fcc derivative superstructures. Thus, the range of the CE was kept within the limits indicated by the HT results. The validity of this reduction is further shown by noting that the lowest energy predicted ground state is at 25 at. % W.

Quantum mechanical energies used in the construction of the CE were computed on an equivalent **k**-point scheme to reduce systematic error. Rh and W pseudopotentials incorporating the semi-core p electrons with an energy cut-off of approximately 271 eV were used. Input energies, CE predictions, and lowest-energy predictions of the ground state search (including fcc superstructures with up to 10 atoms per unit cell) are shown in Fig. 2.4. A canonical Monte Carlo simulation using the Metropolis algorithm was performed on a 20 × 20 × 20 unit cell with periodic boundary conditions. The results, including the specific heat determined using the familiar statistical relation $\sigma_{\mathrm{E}}^2 = \langle \mathrm{E}^2 \rangle - \langle \mathrm{E} \rangle^2$ are shown in Fig. 2.5.

CE-based MC modeling revealed an order-disorder transition temperature between 900–1000 K in the Rh-W system at 8:1 stoichiometry. Experimental Rh-W phase diagrams show the liquidus line near 2200 K at 11 at. % W. It is then conceivable that the A_8B phase could be produced after the introduction of excess vacancies (via charged particle irradiation [60] or cold working [50]), if not by spontaneous ordering alone.

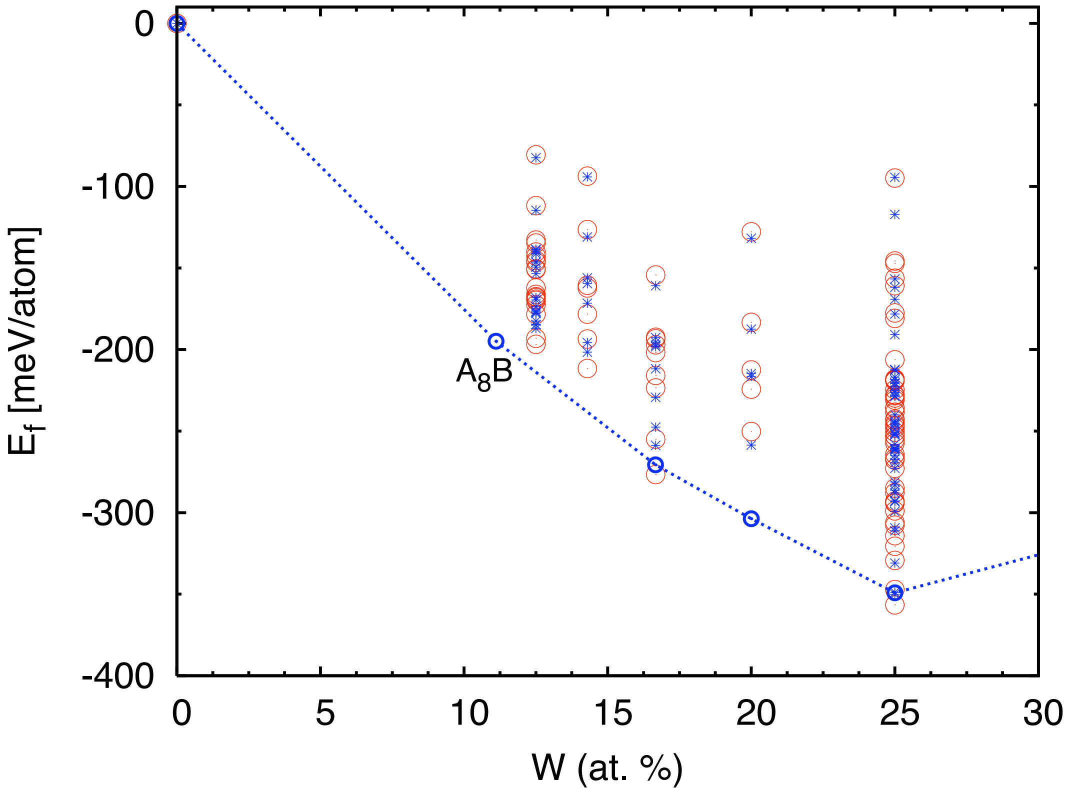

Figure 2.4 CE input energies calclated from first principles (red, large circles) with cluster expansion predictions (blue, stars). The blue tie line connects the stable structures after a ground state search. For clarity, the ground state search enthalpies are not shown *except* for the stable states, the vertices of the convex hull (blue line). The stable state at x=11 at. % W is the 8:1 structure. Input structures with concentrations between 0–25 at. % W were selected because the applicability of an fcc CE approach was established by HT within this range.

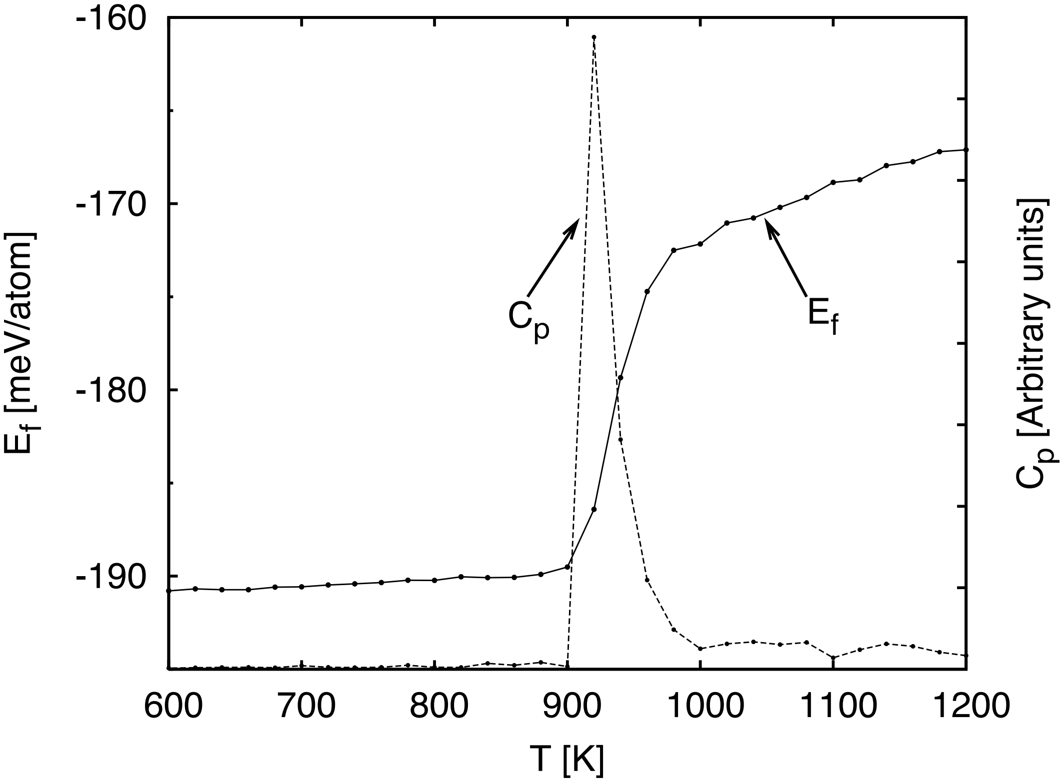

Figure 2.5 Canonical Monte Carlo results at 11 at. % W in Rh-W. Configurational specific heat is overlaid with finite temperature formation enthalpy. The transition is estimated between 900–1000 K.

2.4 Conclusions

In conclusion, using the high-throughput method the A_8B phase was found in 59 systems, 48 of which are yet unobserved. By verifying experiment and previous predictions while also offering *additional* predictions, our results demonstrate the power of the HT approach in a dramatic fashion. Although it is possible that some of the predicted phases may not be observed experimentally due to kinetic limitations, a CE extension to finite temperatures illustrates that the investigation is not merely academic. In the system Rh-W the transition was predicted high enough to be realized experimentally. Further investigation is required to determine the extent to which the remaining predicted phases may be seen experimentally.

Chapter 3

Binary magnesium alloys from first principles

3.1 Introduction

The importance of materials in modern society is difficult to overstate and continues to grow as twenty-first century challenges emerge. Concern over human energy consumption and environmental impact has become urgent in recent years, even making a striking entrance into the public discourse. Paralleling this, the desire for highly efficient materials tailored to specific applications has increased. A great deal of effort has focused on material weight and strength. Light yet durable materials are needed in the automotive and aerospace industries, two sectors that are jointly responsible for the largest source of anthropogenic pollutants and a significant portion of global energy consumption.

Magnesium (Mg) alloys are among the lightest structural materials and are used in a variety of applications (not only in automotive and aerospace manufacturing but also, for example, in electronic device manufacturing). Over the past decade Mg consumption has increased dramatically due in large part to an impetus in the automotive industry for lighter, more energy efficient vehicles. This has been accompanied by an increase of Mg research, and although undeniable progress has been made toward the understanding of the thermodynamic behavior of Mg alloys (see for example Ref. [73] and [74]) much remains to be done.

In improving or designing alloys, materials scientists rely on the thermodynamic information in published phase diagrams. This information is found directly through published phase diagrams and modeling databases such as Calphad.However, thermodynamic data for even common alloys is sometimes incomplete. This is due, at least in part, to the difficulty of achieving thermodynamic equilibrium at low temperatures. First-principles methods provide a powerful tool in this arena and can be used to complete our understanding of the low temperature thermodynamics of alloys.

First-principles methods have long been recognized as a viable approach to the study of materials and have already been applied to a number of systems. Accurate formation enthalpy predictions at zero temperature require only details of the crystal structure and composition; and although calculations of this sort are slow compared to very fast models such as Cluster Expansion, they are not limited to derivative superstructures of a parent lattice. In a *high-throughput* (HT) approach, searches over many crystallographic types can be made, thereby introducing the possibility of finding surprising new (even off-lattice) predictions. Ground state predictions made in this manner are typically in very good agreement with experimental results as shown recently by Curtarolo et al [68] and described in Methods.

Using our HT framework AFLOW, we have explored the full composition ranges of 39 Mg-X binary systems at zero temperature. In nearly one third of the cases, our calculations are entirely consistent with published phase diagrams. That is, the ordered phases shown in the phase diagram coincide exactly with the low temperature ground state predictions of HT approach. In a little more than a third, the differences between the DFT results and phase diagrams are relatively minor (though the differences may still indicate new opportunities for alloy design). Finally, the remaining cases either have no published phase diagrams, or the phase diagram information and calculated ground states differ significantly.

The remainder of the paper progresses as follows. After a discussion of the HT methodology and library, systems in which no ab initio compounds were predicted are reported. Following this, compound forming systems are reported and discussed individually. These are presented in alphabetical order with tables summarizing data related to each. Plots showing formation enthalpy versus atomic percent Mg for each system are also included. Finally, summarizing tables composed of all systems' data and crystallographic information for certain prototypes included in the study are given in the Appendix.

3.2 Methodology and high-throughput library

In the *high-throughput* approach, the ground state behavior of a binary system is studied by the results of a brute force search— formation enthalpies are calculated for essentially every crystal structure ever observed in binary metal systems as well as a large number of enumerated derivative superstructures [67]. This procedure gives reasonable results as shown in Ref. [68] where it was shown that the probability of reproducing the correct ground state, if well defined, not ambiguous, and present in our list of prototypes is $\eta_c^\star \sim 96.7\%$ (*"reliability of the method"*, Eq. (3) of Ref. [68]).

It must be mentioned that there is no guarantee that the true ground states of a system will be found among the common experimentally observed structures or among small-unit-cell derivative structures. However, even if it is impossible to rule out the existence of an unexpected ground state, this procedure (searching many enumerated derivative structures and exhaustively exploring experimentally reported structures) is expected to give a reasonable balance between high-throughput speed and scientific accuracy to determine the $T = 0\,K$ ground states of Mg-X systems.

Calculations were performed using the AFLOW framework [25,28,34,68,69] based on *ab initio* calculations of the energies by the VASP software [70]. We used projector augmented waves (PAW) pseudopotentials [23] and the exchange-correlation functionals parameterized by Perdew, Burke and Ernzerhof [71] for the generalized gradient approximation (GGA). The energies were calculated at zero temperature and pressure (thus energies and enthalpies coincide), with spin polarization and without zero-point motion or lattice vibrations (zero-point motion is negligible because we do not consider light elements). All crystal structures were fully relaxed (cell volume and shape, and atomic positions). Numerical convergence to about ~ 1 meV/atom was ensured by a high energy cutoff (30% higher than the highest energy cutoff for the pseudopotentials of the components) and dense 6000-8000 **k**-point Monkhorst-Pack meshes.

The energies of more than 200 crystal structures were calculated for each of the Mg-X systems studied. In addition to the 176 configurations described in

[68], these included all the symmetrically-distinct hcp-, bcc-, fcc-based superstructures [67] with up to four atoms per cell, and the prototypes A5, A6, A7, A8, A9, A11, B20, C36, D5_{19}, Al_2Zr_4, Al_3Zr_2, CdTi, $CuPt_7$, Cu_3Ti_2, Ga_2Hf, Ga_4Ni, Ga_3Pt_5, Ga_4Ti_5, Hg_2Pt, ITl, InTh, LiB-MS1/2 [31,72], $NbNi_8$(Pt_8Ti), $NiTi_2$, SeTl and V_4Zn_5. The additional prototypes were considered because they are common or related to noble metal alloys [32,33]. We did not consider lattice-superstructures with more than four atoms per cell due to the fact that their number increases enormously

The solute atoms considered in this study are the following: Ag, Al, Au, Ca, Cd, Cu, Fe, Ga, Ge, Hf, Hg, In, Ir, K, La, Li, Mo, Na, Nb, Os, Pb, Pd, Pt, Rb, Re, Rh, Ru, Sc, Si, Sn, Sr, Ta, Tc, Ti, V, W, Y, Zn, Zr. To out knowledge, this constitutes the largest unified study of Mg alloys. Most of the transition metals and several other alloys of industrial importance (X=Al, Ca, Ge, K, Pb, Si, Sn, Y) are included.

3.3 Phase-separating systems

The following systems produced no compounds: Fe-Mg, Mg-Mo, Mg-Nb, Mg-Os, Mg-Re, Mg-Ta, Mg-Ti, Mg-V, and Mg-W. Systems shown to be phase separating by all positive ab intio enthalpy calculations were in every case also reported to be phase separating experimentally. The converse, however, was not always true. Several systems previously believed to be phase separating produced thermodynamically stable compounds. These systems are included in what follows.

3.4 Alloys with *ab initio* compounds

Although the system tables are intended to be more or less self-explanatory a few clarifying details are in order: System tables include all low-temperature experimental and $T=0\,\mathrm{K}$ ab initio ground states. The compounds are reported in order of increasing Mg content, with concentration given in column I, experimental results given in column II, and ab initio results given in column III. Relative enthalpies are given in instances of a) very close competing (in energy) phases, b) when experimental phases are many meV/atom above the ab initio ground state, or c) an ab initio ground state does not exist. In non-compound forming systems with ab initio ground states, the formation enthalpy (Δ H) is given relative to zero. In systems without assessed phase diagrams, experimental results are indicated by a dash (—) when compared to ab initio results. Experimental phases with unit cell sizes too large to compute with ab initio methods are indicated by three asterisks (***). If the the experimental compound is undetermined, this is noted by *unknown*. Structures marked with an asterisk (e.g., Be_2Zn-65*) are relaxed lattice-derived prototypes and are described in the Structure Tables in the Appendix.

Ag-Mg

Ab initio compounds vary slightly from experimental phases in the Ag-Mg system. The compound Ag_3Mg is reported to be Cu_3Au-$L1_2$ while ab initio calculations show Al_3Zr-$D0_{23}$ to be the lowest energy state at $T=0\,K$. $L1_2$ and $D0_{22}$ are structurally similar to $D0_{23}$—the three differ by the periodicity of an antiphase boundary, and are relatively close in energy at $T=0\,K$, according to ab initio results.

Although there is experimental consensus regarding the structure of MgAg—

CsCl-B2—ab initio results predict B2 slightly higher in energy than CuAu-$L1_0$, the predicted ground state. B2 is related to $L1_0$ by a simple distortion of the unit cell, so a low temperature transformation martensitic type may occur. The ab initio compound $AgMg_2$ with the $NiTi_2$ structure has not been found experimentally. Two phases of unspecified crystallographic properties are reported in experimental phase diagrams at compositions $AgMg_3$ and $AgMg_4$ and could not be included in the HT database. Ab initio ground states are not predicted at these compositions.

Composition % Mg	Experimental results	Ab initio results
25.0	$AuCu_3$-$L1_2$	Al_3Zr-$D0_{23}$ MgAu3±x ~3.0 meV Al_3Ti-$D0_{22}$ ~4.5 meV/atom $AuCu_3$-$L1_2$ ~8.4 meV/atom *above* $D0_{23}$
50.0	CsCl-B2	CsCl-B2
66.6	*two-phase region*	$NiTi_2$
75.0	$AgMg_3$ *unknown*	$Cu_{2.82}P$-$D0_{21}$ Ni_3Sn-$D0_{19}$ ~14.8 meV/atom *above* $D0_{21}$
80.0	$AgMg_4$ *unknown*	*two-phase region* $f_{52}^{\dagger}$ ~29.1 meV/atom *above tie line*

Table 1 The Ag-Mg system. (†) See Structure Tables for crystallographic description. Experimental data taken from [33, 75–83].

Al-Mg

No simple compounds (few atoms in the unit cell) are reported to form in the Al-Mg system. Two low-temperature compounds of complex structure are reported: $Al_{12}Mg_{17}$, $Al_{45}Mg_{28}$. Due to its complexity (>1000 atoms in the unit cell), the $Al_{45}Mg_{28}$ structure was not included in the structure database. The $Al_{12}Mg_{17}$ structure was included, however the calculated formation enthalpy is not low enough to be a thermodynamic minimum. The hcp-derived prototype,

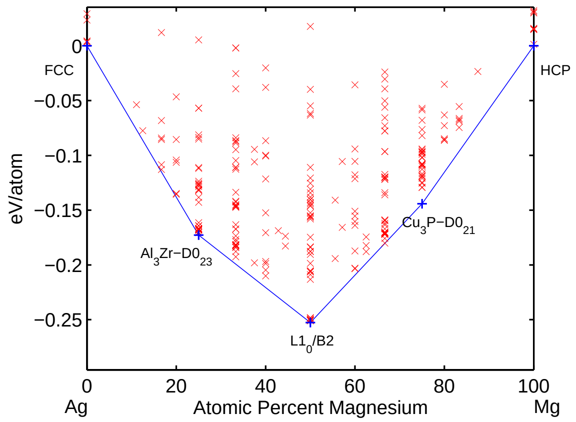

Figure 3.1 Ag-Mg convex hull. Ground states are labeled by the prototype and the Struckturbericht designation, if one exists.

Be_2Zn-65 (See Structure Table), is the T=0 K ab initio ground state and is significantly lower in energy than all negative-enthalpy competitors. Ab initio calculations give only a few additional results with negative enthalpy of formation: C14, C15, and C36 (composition Al_2Mg) and the $Al_{12}Mg_{17}$ structure.

Composition % Mg	Experimental results	Ab initio results
33.3	*two-phase region*	Be$_2$Zn-65*† MgNi$_2$-C36 ∼590 meV/atom MgZn$_2$-C14 ∼591 meV/atom Cu$_2$Mg-C15 ∼595 meV/atom *above* Be$_2$Zn-65*
38.4	Al$_{45}$Mg$_{28}$	*two-phase region*
58.6	Al$_{12}$Mg$_{17}$	*two-phase region* Al$_{12}$Mg$_{17}$ ∼928 meV/atom *above tie line*
66.6	*two-phase region*	Be$_2$Zn-65*

Table 2 The Al-Mg system. (†) See Structure Tables for crystallographic description. Experimental data taken from [33, 84–107].

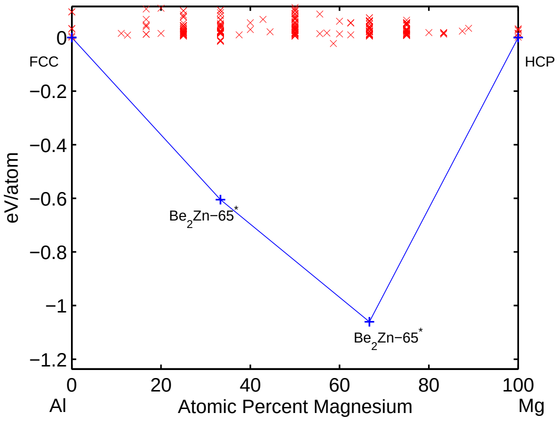

Figure 3.2 Al-Mg convex hull. Ground states are labeled by the prototype and the Struckturbericht designation, if one exists.

Au-Mg

There are several low-temperature experimental phases in the Au-Mg system: Al_3Zr-$D0_{23}$, CsCl-B2, $AuMg_2$ and Cu_3P-$D0_{21}$. Ab initio data confirms the experimental phases and predicts an additional phase at composition Au_3Mg_5. The high-temperature phase at composition Au_3Mg is stable at T = 0 K.

Composition % Mg	Experimental results	Ab initio results
16.6	*solid solution*	$HfPd_5$-141*†
25.0	$MgAu_{3-x}/MgAu_{3+x}$ Al_3Zr-$D0_{23}$ *high-temperature*	$MgAu_{3-x}/MgAu_{3+x}$ Al_3Zr-$D0_{23}$ ∼3.4 meV/atom *above* $MgAu_{3-x}$
50.0	CsCl-B2	CsCl-B2/$L1_0$
62.5	*two-phase region*	Si_3W_5
66.6	$AuMg_2$	$AuMg_2/Co_2Si$-C37 *above* $AuMg_2$
75.0	$Cu_{2.82}P$-$D0_{21}$	$Cu_{2.82}P$-$D0_{21}$

Table 3 The Au-Mg system. (†) See Structure Tables for crystallographic description. Experimental data taken from [33, 108–110].

Ca-Mg

Ca-Mg is a simple system having one intermetallic compound. The experimental phase is found at composition $CaMg_2$ with the $MgZn_2$-C14 structure. Experimental phase diagrams show the phase melts congruently. Ab initio

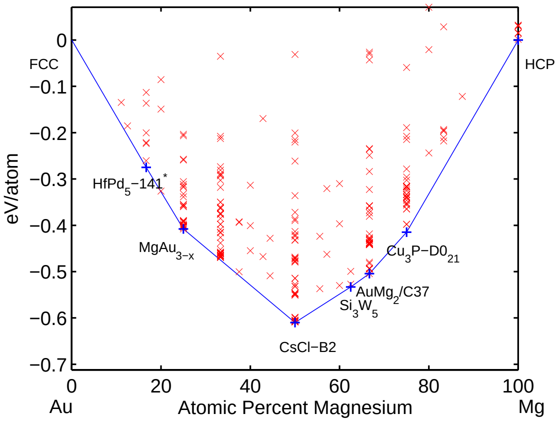

Figure 3.3 Au-Mg convex hull. Ground states are labeled by the prototype and the Struckturbericht designation, if one exists.

calculations result in a single ground state at the same composition and with the same structure.

Composition % Mg	Experimental results	Ab initio results
66.6	$MgZn_2$-C14	$MgZn_2$-C14
		$MgNi_2$-C36 ∼2.3 meV/atom
		Cu_2Mg-C15 ∼4.2 meV/atom
		above C14

Table 4 The Ca-Mg system. Experimental data taken from [33, 111–117].

Cd-Mg

Experimental phase diagrams show intermetallic compounds at compositions Cd_3Mg, CdMg, and $CdMg_3$. Ab initio ground states are found at the same compositions with identical structural properties.

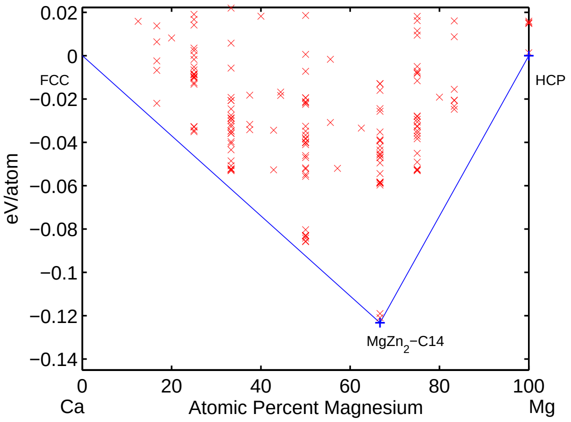

Figure 3.4 Ca-Mg convex hull. Ground states are labeled by the prototype and the Struckturbericht designation, if one exists.

Composition % Mg	Experimental results	Ab initio results
25.0	Cd_3Mg	Cd_3Mg
50.0	AuCd-B19	AuCd-B19 AuCu-$L1_0$ ∼8.7 meV/atom *above* B19
75.0	$CdMg_3$	$CdMg_3$

Table 5 The Cd-Mg system. Experimental data taken from [33, 118–133].

Cu-Mg

Ab initio ground states in the Cu-Mg system agree with experiment. Experimental phase diagrams show intermetallic compounds at compositions Cu_2Mg and $CuMg_2$. The phases melt congruently. Given the agreement of the T = 0 K ab initio predictions, the finite temperature experimental phases are likely stable from T = 0 K to the melting temperatures.

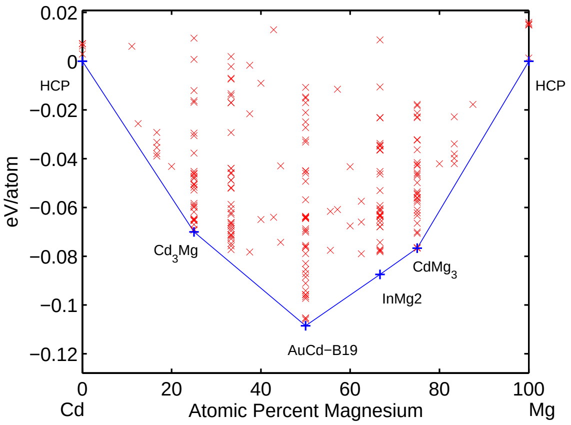

Figure 3.5 Cd-Mg convex hull. Ground states are labeled by the prototype and the Struckturbericht designation, if one exists.

Composition % Mg	Experimental results	Ab initio results
33.3	Cu_2Mg-C15	Cu_2Mg-C15 $MgNi_2$-C36 ∼0.9 meV/atom $MgZn_2$-C14 ∼2.1 meV/atom *above* C15
66.6	Al_2Cu-C16	Al_2Cu-C16

Table 6 The Cu-Mg system. Experimental data taken from [33, 134–138].

Ga-Mg

Ab initio compounds differ from observed experimental ground states in the Ga-Mg system. The ab initio ground state Be_2Zn-65* was included in the HT database because it is a relaxed simple hcp-derived superstructure (see Structure Tables). The phase was first predicted in the system Be-Zn [139]. Nearest-in-energy phases are many meV above Be_2Zn-65* providing

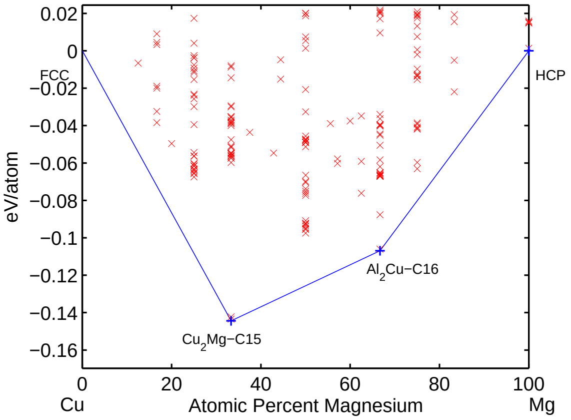

Figure 3.6 Cu-Mg convex hull. Ground states are labeled by the prototype and the Struckturbericht designation, if one exists.

convincing evidence for thermodynamic stability of the Be_2Zn-65* phase at finite temperature.

Composition % Mg	Experimental results	Ab initio results
28.5	Mg_2Ga_5 *SG #139*	*two-phase region* Mg_2Ga_5 ∼118.0 meV/atom *above tie line*
33.3	$MgGa_2$ *SG #55*	Be_2Zn-65*† $MgGa_2$ ∼141.2 meV/atom *above* Be_2Zn-65*
66.6	Mg_2Ga *SG#190*	Be_2Zn-65* $MgGa_2$ ∼139.1 meV/atom *above* Be_2Zn-65
71.4	Mg_5Ga_2 *SG #72*	*two-phase region* Mg_5Ga_2 ∼247.9 meV/atom *above tie line*

Table 7 The Ga-Mg system. (†) See Structure Tables for crystallographic description. Experimental data taken from [33, 140–144].

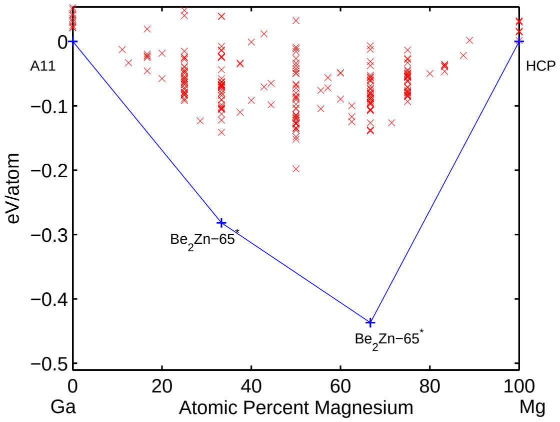

Figure 3.7 Ga-Mg convex hull. Ground states are labeled by the prototype and the Struckturbericht designation, if one exists.

Ge-Mg

A single ab initio ground state is predicted in the Ge-Mg system at composition Ge_2Mg, in agreement with experimental phase diagrams. However, the crystal structure of the ab initio phase Be_2Zn-65* (see Structure Tables) differs from the experimental phase (CaF_2). The Be_2Zn-65* phase is ∼300 meV/atom lower than CaF_2, the next-lowest in energy phase.

Composition % Mg	Experimental results	Ab initio results
66.6	CaF_2	Be_2Zn-65*†
		CaF_2 ∼292.4 meV/atom
		above Be_2Zn-65

Table 8 The Ge-Mg system. (†) See Structure Tables for crystallographic description. Experimental data taken from [33, 145–148].

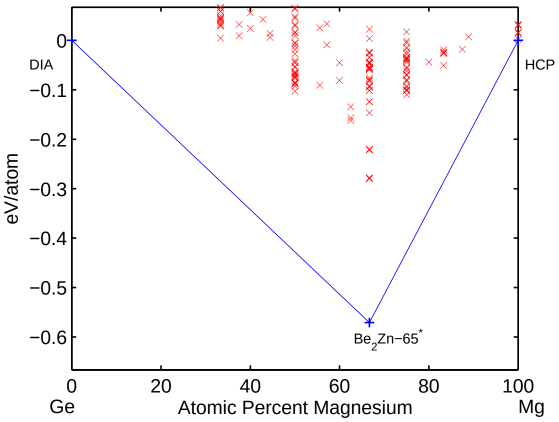

Figure 3.8 Ge-Mg convex hull. Ground states are labeled by the prototype and the Struckturbericht designation, if one exists.

Hf-Mg

The Hf-Mg system has been investigated by Levy, Hart and Curtarolo [149].

For completeness the data will also be reported here.

Composition % Mg	Experimental results	Ab initio results
50.0	*non-compound* *forming*	CdTi ∼5.9 meV/atom *below* $\Delta H = 0$

Table 9 The Hf-Mg system.

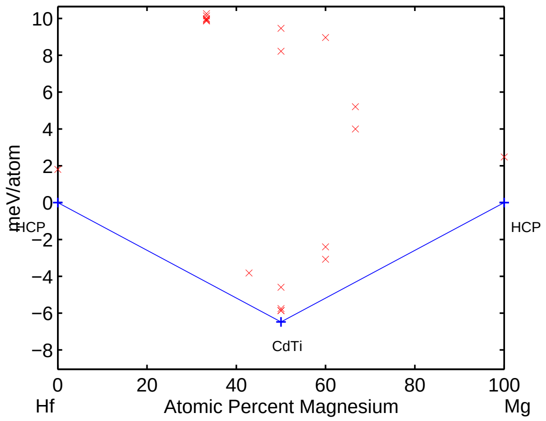

Figure 3.9 Hf-Mg convex hull. Ground states are labeled by the prototype and the Struckturbericht designation, if one exists.

Hg-Mg

Several line compounds have been identified by experiment in the Hg-Mg system. In large part, these are verified by HT quantum mechanical calculations. The unidentified phase at composition Hg_3Mg_5 is not supported by HT results and could not be evaluated directly because the structure is unknown. Whether a phase is stable at $T = 0(K)$ at this composition or not is unclear as only a limited number of structures with the appropriate composition exist in the database. The phase at composition Mg_3Hg is not thermodynamically stable at $T = 0(K)$ according to ab initio data. The lowest energy ab initio phase at this composition is not the experimental phase.

Composition % Mg	Experimental results	Ab initio results
33.3	$MoSi_2$-$C11_b$	Si_2Th-C_c ~2.0 meV/atom *above tie line* Co_2Si-C37 ~21.4 meV/atom $C11_b$ ~22.0 meV/atom *above* C_c
50.0	CsCl-B2	CsCl-B2/$L1_0$ NiTi ~1.7 meV/atom *above* B2
62.5	Mn_5Si_3-$D8_8$	Mn_5Si_3-$D8_8$
66.6	Co_2Si-C37	Co_2Si-C37 Fe_2P-C22 ~3.9 meV/atom
71.4	Mg_5Hg_2 *unknown*	*two-phase region*
75.0	Mg_3Hg	*two-phase region* $D0_{19}$ ~3.8 meV/atom *above tie line* Mg_3Hg ~28.5 meV/atom *above* $D0_{19}$

Table 10 The Hg-Mg system. Experimental data taken from [33, 150–152].

In-Mg

The ab initio ground states in the In-Mg system differ significantly from experimental phases. The T = 0(K) formation enthalpy of the experimental

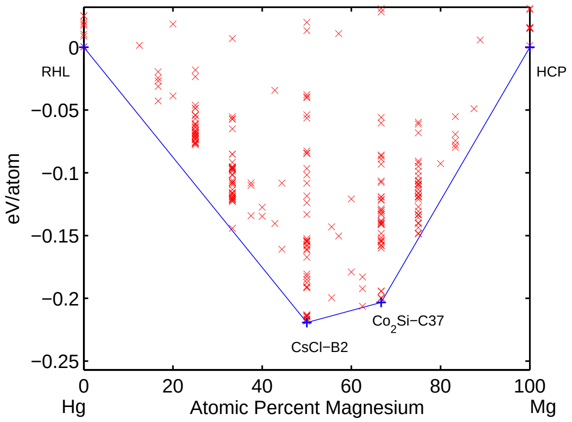

Figure 3.10 Hg-Mg convex hull. Ground states are labeled by the prototype and the Struckturbericht designation, if one exists.

phases is not low enough in most cases to result in thermodynamic stability. At those compositions where experimental phases are also found, ab initio ground states are predicted at compositions InMg, $InMg_2$, and $InMg_3$. However, the structural properties of the predicted phases do not always agree with experiment. In particular, the experimental phase at composition $InMg_2$, ∼5 meV above the ab initio ground state, undergoes a symmetry raising to space group P63/mmc #194. An additional phase is predicted at composition In_3Mg with the Si_2Th-C_c structure; no experimental phase is reported at this concentration.

Composition % Mg	Experimental results	Ab initio results
25.0	Cu_3Au-$L1_2$	*two-phase region* $L1_2$ ∼9.0 meV/atom *above tie line*
33.3	*two-phase* *region*	Si_2Th-C_c Ga_2Hf ∼14.5 meV/atom *above* C_c
50.0	AuCu-$L1_0$	AuCu-$L1_0$
66.6	$InMg_2$	Ga_2Hf *metastable* Fe_2P-C_{22} ∼4.5 meV/atom *above* Ga_2Hf
71.4	Ga_2Mg_5	*two-phase region* Ga_2Mg_5 ∼7.8 meV/atom *above tie line*
75.0	$InMg_3$	$InMg_3$

Table 11 The In-Mg system. Experimental data taken from [33,153–159].

Ir-Mg

Although Ir is rare and costly, it is possessed of remarkable physical and chemical properties [160]. Ironically, the very same properties that make it a material of practical interest (high melting point, resistance to corrosion, etc.) are responsible for the little that is known about its alloys.

Ir-Mg is no exception, and experimental phase diagrams for this system are not complete. Data is especially sparse at low temperatures because of the

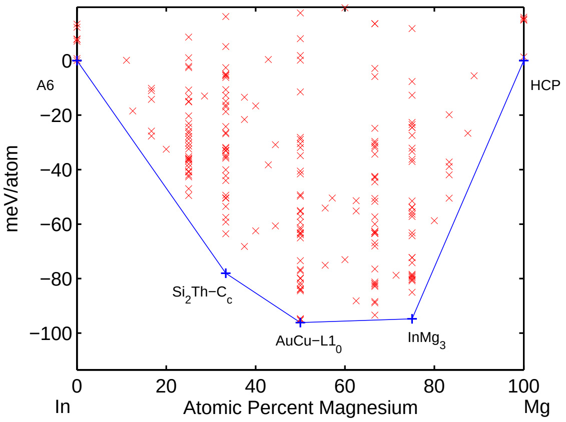

Figure 3.11 In-Mg convex hull. Ground states are labeled by the prototype and the Struckturbericht designation, if one exists.

high melting point (data is only reported to ∼850 K). Experimental Ir-rich phases are nonexistent, the most Ir-rich phase found at composition Mg_3Ir. Here again, the remarkable properties of Ir—in particular, its great stability—are to blame.

Ab initio predictions are then quite interesting. In summary, two Ir-rich phases are found: the fcc derived Ca_7Ge structure at composition Ir_7Mg and an hcp-derived prototype [139], Re_3Ru-124. An fcc derived structure with A_2B_2 stacking along [311] is thermodynamically stable at composition IrMg. We are able to report with less certainty the Mg-rich phases. The experimental phase $Mg_{44}Ir_7$ was not evaluated with first-principles because of the large unit cell size. Also, the structural details of the reported phase at composition $IrMg_4$ are not known. Nevertheless, the ab initio phase at composition $IrMg_3$ confirms the experimental phase.

Composition % Mg	Experimental results	Ab initio results
12.5	—	Ca_7Ge
25.0	—	Re_3Ru-124*† $CdPt_3$ ∼62.3 meV/atom *above* Re_3Ru-124*
50.0	—	17†
75.0	Cu_3P-$D0_{21}$	Cu_3P-$D0_{21}$
80.0	Mg_4Ir *unknown*	*two-phase region* $MoNi_4$-$D1_a$ ∼65.0 meV/atom *above tie line.*
86.2	$Mg_{44}Ir_7$	***

Table 12 The Ir-Mg system. (†) See Structure Tables for crystallographic description. Experimental data taken from [33, 161].

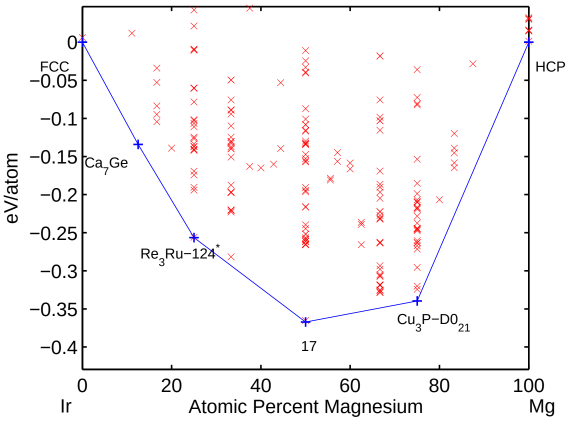

Figure 3.12 Ir-Mg convex hull. Ground states are labeled by the prototype and the Struckturbericht designation, if one exists.

K-Mg

No experimental compounds have been found in the K-Mg system. With one exception, ab initio formation enthalpies are positive. An ab initio compound is found at composition KMg_3.

Composition % Mg	Experimental results	Ab initio results
75.0	*non-compound forming*	$73^{\dagger}$

Table 13 The K-Mg system. (†) See Structure Tables for crystallographic description. Experimental data taken from [162].

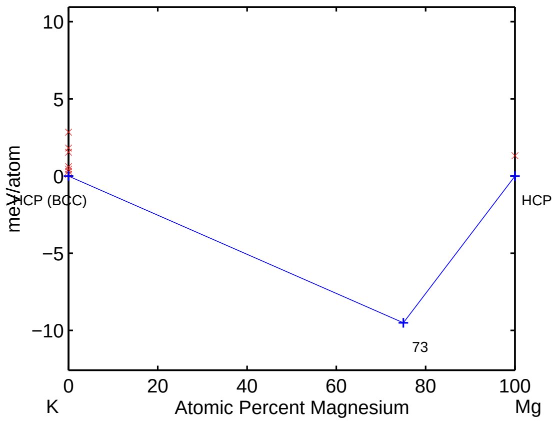

Figure 3.13 K-Mg convex hull. Ground states are labeled by the prototype and the Struckturbericht designation, if one exists.

La-Mg

Ab initio predictions confirm experimental phases at composition LaMg and $LaMg_3$. There is no structural data for the experimental phase at composition $LaMg_{12}$ and an ab initio energy could not be obtained. The phase with the Th_2Ni_{17} structure has positive formation enthalpy. No La-rich phases have been observed experimentally. An ab initio phase is found at composition La_7Mg.

Composition % Mg	Experimental results	Ab initio results
12.5	*two-phase region*	Ca_7Ge
50.0	CsCl-B2	CsCl-B2 NiTi ~4.4 meV/atom *above* B2
75.0	$AlFe_3$-$D0_3$	$AlFe_3$-$D0_3$ Ni_3Sn-$D0_{19}$ ~42.3 meV/atom *above* $D0_3$.
~89.5	Th_2Ni_{17}	Th_2Ni_{17}
~92.3	$LaMg_{12}$ *unknown*	*two-phase region*

Table 14 The La-Mg System. Experimental data taken from [33, 163–168].

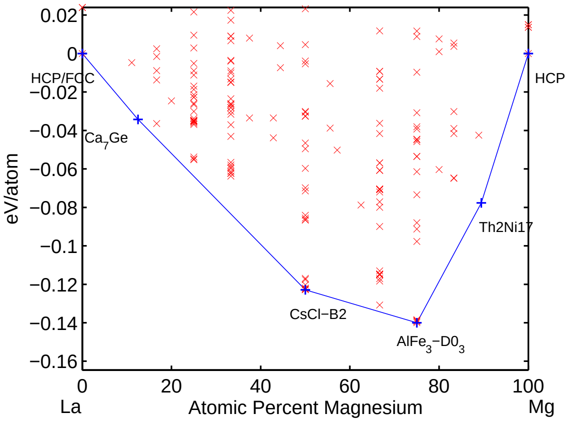

Figure 3.14 La-Mg convex hull. Ground states are labeled by the prototype and the Strukturbericht designation, if one exists.

Li-Mg

The authors have reported ab initio data on the Li-Mg system previously [169]. No intermetallic compounds have been found by experiment. The authors' cluster expansion analysis (*Ibid.*) suggests that the phases may be cryogenic.

Composition	Experimental	Ab initio
% Mg	results	results
20.0	*solid solution*	$\mathrm{MoNi_4}$-$\mathrm{D1}_a$
33.3	*solid solution*	$\mathrm{C49/C11}_b$
50.0	*solid solution*	B2/MoTi*
66.6	*solid solution*	$\mathrm{MoSi_2}$-$\mathrm{C11}_b$ C49 ($\mathrm{ZrSi_2}$) ~6.2 meV/atom above $\mathrm{C11}_b$

Table 15 The Li-Mg system. Experimental data taken from [33,170–179].

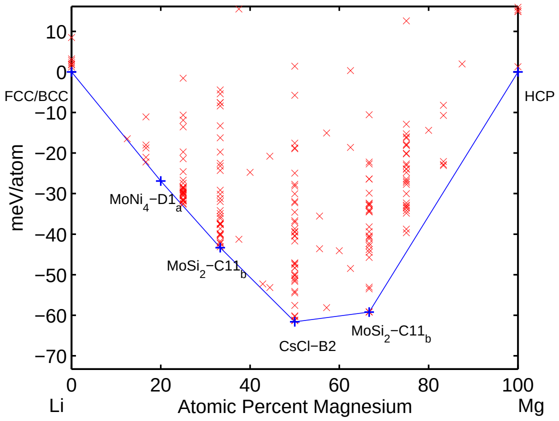

Figure 3.15 Li-Mg convex hull. Ground states are labeled by the prototype and the Struckturbericht designation, if one exists.

Mg-Pb

Experimental phase diagrams indicate a single intermetallic compound at composition Mg_2Pb with the flourite structure, CaF_2. Ab initio calculations reveal additional phases at compositions $MgPb_5$ and Mg_3Pb.

Composition % Mg	Experimental results	Ab initio results
16.6	*two-phase region*	Hf_5Pb-f63*†
66.6	CaF_2	*two-phase reigion* CaF_2 ~7.3 meV/atom *above tieline*
75.0	*two-phase region*	$AuCu_3$-$L1_2$ Co_3V ~2.4 meV/atom *above* $L1_2$

Table 16 The Mg-Pb System. (†) See Structure Tables for crystallographic description. Experimental data taken from [33, 180–187].

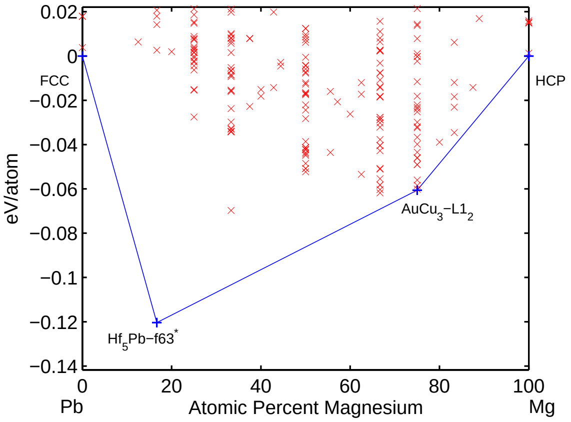

Figure 3.16 Mg-Pb convex hull. Ground states are labeled by the prototype and the Strukturbericht designation, if one exists.

Mg-Pd

Experimental phase diagrams show ∼20 at.% Mg solid solubility in Pd. No Pd-rich intermetallic compounds have been found. The Pd-rich ab initio compounds at compositions $MgPd_3$, and $MgPd_2$ are possibly cryogenic. Regardless, it is unlikely (because the set of AB structures in the HT database is large and diverse) that at least one phase in this region is not stable.

Two experimental phases have been identified at composition MgPd (indicated in Table 17): CuTi forms slightly off stoichiometry at composition $Mg_{0.9}Pd_{1.1}$ and is the only intermediate phase to melt congruently. The CsCl phase forms stoichiometrically and undergoes a peritectic decomposition at ∼970 K. Crystallographic data is not available for the phases at compositions Mg_4Pd and $Mg_{85}Pd_{14}$. The lack of ab initio ground states is inconclusive here as we were unable to evaluate the formation enthalpies for these phases.

Composition % Mg	Experimental results	Ab initio results
12.5	*two-phase region*	Ca_7Ge
20.0	*two-phase region*	$MoNi_4$-$D1_a$
25.0	*two-phase region*	Al_3Zr-$D0_{23}$ Al_3Ti-$D0_{22}$ ∼8.2 meV/atom *above* $D0_{23}$
33.3	*two-phase region*	Co_2Si-C37
37.5	*two-phase region*	Ga_3Pt_5
50.0	CsCl-B2 & CuTi	AuCu-$L1_0$/CsCl-B2 CuTi-B11 ∼230.2 meV/atom *above* $L1_0$
66.6	*two-phase region*	$NiTi_2$/Al_2Cu-C16
∼71.4	Co_2Al_5	Co_2Al_5
75.0	$IrAl_3$-$D0_{18}$	$Cu_{2.82}P$-$D0_{21}$
80.0	Mg_4Pd *unknown*	*two-phase region* $MoNi_4$-$D1_a$ ∼53.9 meV/atom *above tie line*
∼85.7	$Mg_{85}Pd_{14}$ *unknown*	*two-phase region*

Table 17 The Mg-Pd system. Experimental data taken from [33,188].

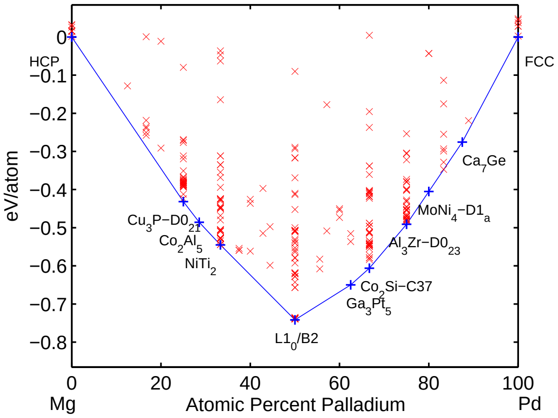

Figure 3.17 Mg-Pd convex hull. Ground states are labeled by the prototype and the Struckturbericht designation, if one exists.

Mg-Pt

The experimental ground states at compositions $MgPt_7$ and Mg_6Pt were not evaluated with ab initio methods. The first, because the structure has not been completely determined, the second, because the cell size is large, exceeding 400 atoms in the unit cell. However, the ab initio ground state Ca_7Ge is at least somewhat consistent with the experimental phase $MgPt_7$: Ca_7Ge is a doubling of the $L1_2$ structure when the 4b Wyckoff position is replaced by a Ge atom and the experimental ground state $MgPt_7$ consists of eight $L1_2$-type cells. At compositions Mg_2Pt and $MgPt_2$ ab initio ground states exist where no experimental phases have been observed. $MgPt_2$ with the Ga_2Hf structure is close to the tie line (∼1.9 meV above the tie line between adjacent ground states) and may be metastable.

Composition % Mg	Experimental results	Ab initio results
12.5	$MgPt_7$[a] *unknown*	Ca_7Ge
25.0	$AuCu_3$-$L1_2$	$AuCu_3$-$L1_2$
33.3	—	Ga_2Hf
50.0	FeSi-B20	AuCu-$L1_0$ NiTi ∼23.9 meV/atom CsCl-B2 ∼31.2 meV/atom FeSi-B20 ∼149.2 meV/atom *above* $L1_0$
66.6	—	Al_2Cu-C16 $NiTi_2$ ∼10.7 meV/atom *above* C16
75.0	Na_3As-$D0_{18}$	$Cu_{2.82}P$-$D0_{21}$ Fe_3C-$D0_{11}$ ∼12.0 meV/atom Na_3As-$D0_{18}$ ∼18.5 meV/atom *above* $Cu_{2.82}P$-$D0_{21}$
∼85.7	Mg_6Pt	***

Table 18 The Mg-Pt system. (a) This structure has been shown to consist of eight $L1_2$-type cells [189]. Experimental data taken from [33].

Mg-Na

No intermetallic phases have been observed in the Mg-Na system. An ab initio ground state is predicted at composition Mg_3Na_5 with the Al_3Zr_2 structure. Additional compounds with negative formation enthalpy (not sufficiently

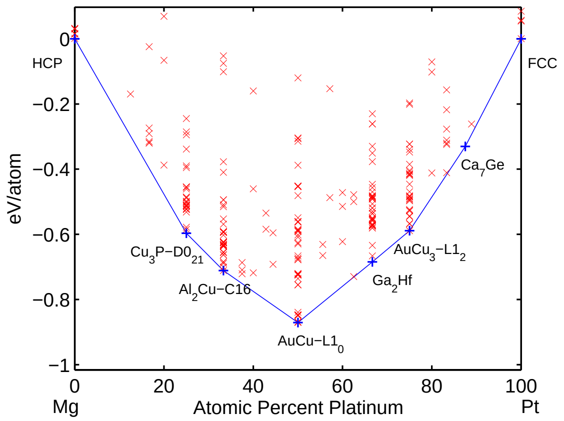

Figure 3.18 Mg-Pt convex hull. Ground states are labeled by the prototype and the Strukturbericht designation, if one exists.

negative to be ground states) are found at compositions $MgNa_3$, Mg_2Na_3, and Mg_3Na_2 .

Composition % Mg	Experimental results	Ab initio results
60.0	*non-compound forming*	Al_3Zr_2 ~223.9 meV/atom *below* $\Delta H = 0$ Bi_2Te_3 ~199.5 meV/atom *above* Al_3Zr_2

Table 19 The Mg-Na system. Experimental data taken from [33].

Mg-Rb

No intermetallic phases have been observed in the Mg-Rb system. An ab initio ground state is predicted at composition Mg_3Rb. The ground state phase, also the only structure with calculated negative formation enthalpy, is a simple bcc-derived superstructure (see Structure Tables).

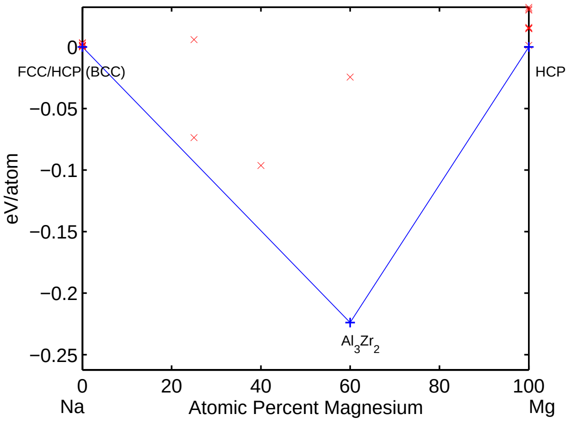

Figure 3.19 Mg-Na convex hull. Ground states are labeled by the prototype and the Strukturbericht designation, if one exists.

Composition % Mg	Experimental results	Ab initio results
75.0	*non compound forming*	73† ∼396.2 meV/atom *below* $\Delta H = 0$ $\beta Cu_3Ti\text{-}D0_a$ ∼580.1 meV/atom *above* 73

Table 20 The Mg-Rb System. (†) See Structure Tables for crystallographic description. Experimental data taken from [33].

Mg-Rh

Due to a large unit cell (more than 400 atoms) the experimental phase $Mg_{44}Rh_7$ was not evaluated using first principles. Although, the phase diagram has not been determined in the Mg-Rh system, two additional experimental phases have been observed—Mg_5Rh_{2-x} and MgRh. The non-stoichiometric compound (prototype Al_5Co_2) was evaluated with first principles.

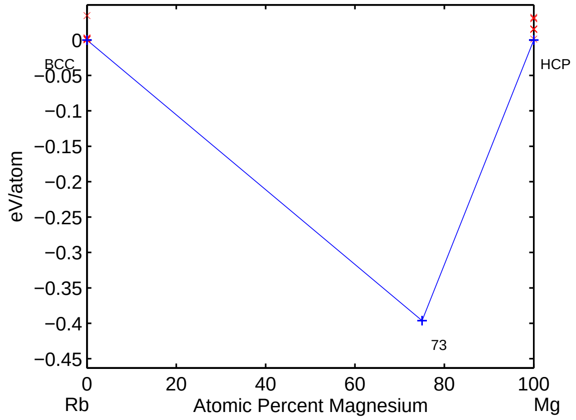

Figure 3.20 Mg-Rb convex hull. Ground states are labeled by the prototype and the Struckturbericht designation, if one exists.

Composition % Mg	Experimental results	Ab initio results
12.5	—	Ca_7Ge
25.0	—	Re_3Ru-124*† Al_3Ti-$D0_{22}$ ∼30 meV/atom *above* Re_3Ru-124
50.0	CsCl-B2	CsCl-B2
66.6	—	Hf_2Tl-6*$^{\dagger b}$ $NiTi_2$ ∼17.8 meV/atom *above* Hf_2Tl-6*
∼71.4	Al_5Co_2	Al_5Co_2
75.0	—	$Cu_{2.82}P$-$D0_{21}$
∼86.3	$Mg_{44}Rh_7$	*two-phase region*

Table 21 The Mg-Rh System. (†) See Structure Tables for crystallographic description. (b) Tetragonal distortion of β_2 [149]. Experimental data taken from [33].

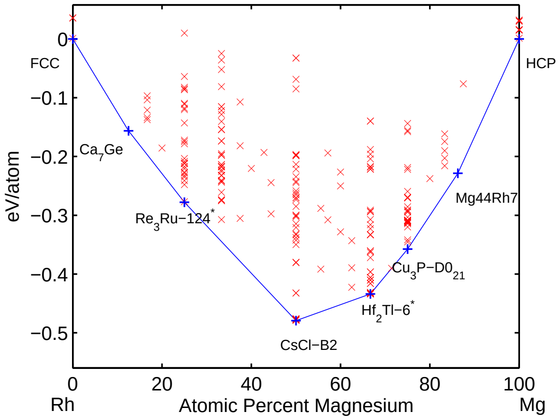

Figure 3.21 Mg-Rh convex hull. Ground states are labeled by the prototype and the Strukturbericht designation, if one exists.

Mg-Ru

Very little published data exists regarding the Mg-Ru system. The phase diagram has not been determined. Two experimental intermetallic phases are observed at compositions Mg_3Ru_2 and $Mg_{44}Rh_7$. An ab initio ground state is found at composition Mg_3Ru.

Composition % Mg	Experimental results	Ab initio results
60.0	Mg_3Ru_2	Mg_3Ru_2
∼86.3	$Mg_{44}Rh_7$	***

Table 22 The Mg-Ru system.

Mg-Sc

Ab initio predictions for the Mg-Sc system differ somewhat from data reported in experimental phase diagrams. A single intermetallic compound, CsCl-B2, is reported while three ab initio phases exist. Additionally, the CsCl phase is found to be higher in formation enthalpy at T=0 K than the ab initio

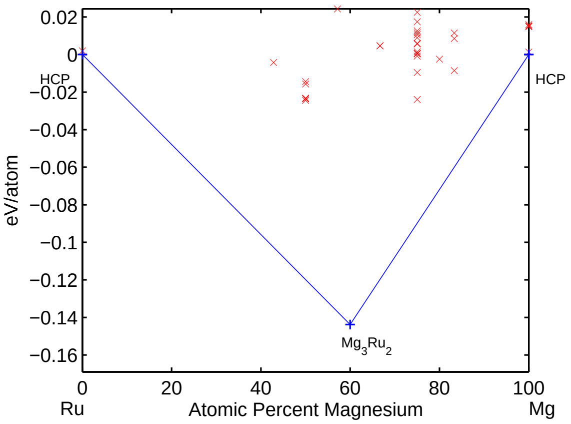

Figure 3.22 Mg-Ru convex hull. Ground states are labeled by the prototype and the Strukturbericht designation, if one exists.

ground state CdTi. The two additional ab initio phases occur at compositions $MgSc_2$ and Mg_3Sc.

Composition % Mg	Experimental results	Ab initio results
33.3	*two-phase region*	Si_2Zr-C49 $FCC_{AB2}{}^{[100]}$-$\beta2$ ∼3.9 meV/atom *above* C49
50.0	CsCl-B2	CdTi CsCl-B2 ∼5.9 meV/atom *above* CdTi
75.0	*two-phase region*	Ni_3Sn-$D0_{19}$ $AuCu_3$-$L1_2$ ∼2.0 meV/atom *above* $D0_{19}$

Table 23 The Mg-Sc system. Experimental data taken from [33,190].

Mg-Si

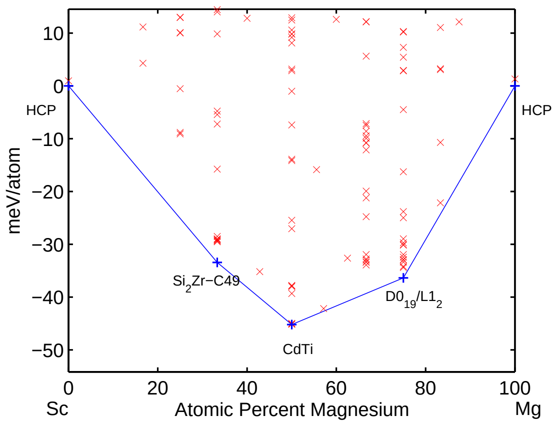

Figure 3.23 Mg-Sc convex hull. Ground states are labeled by the prototype and the Struckturbericht designation, if one exists.

Stability of the experimental compound at Mg_2Si is not corroborated by ab initio calculations. The Be_2Zn*-65 structure is found to have significantly lower formation enthalpy and is a ground state at compositions Mg_2Si and $MgSi_2$.

Composition % Mg	Experimental results	Ab initio results
33.3	*two-phase region*	Be_2Zn-65*†
66.6	CaF_2	Be_2Zn-65* CaF_2 ∼812 meV/atom *above* Be_2Zn-65*

Table 24 The Mg-Si system. (†) See Structure Tables for crystallographic description. Experimental data taken from [33, 191–197].

Mg-Sn

A single ab initio ground state is found in the Mg-Sn system and occurs at

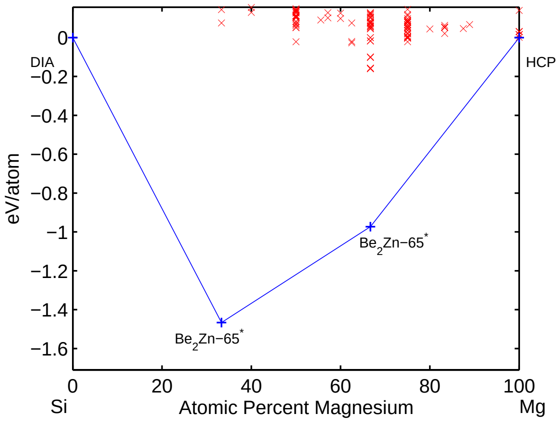

Figure 3.24 Mg-Si convex hull. Ground states are labeled by the prototype and the Struckturbericht designation, if one exists.

the same composition as the experimental compound: Mg_2Sn.

Composition % Mg	Experimental results	Ab initio results
66.6	CaF_2	CaF_2

Table 25 The Mg-Sn system. Experimental data taken from [33,198–208].

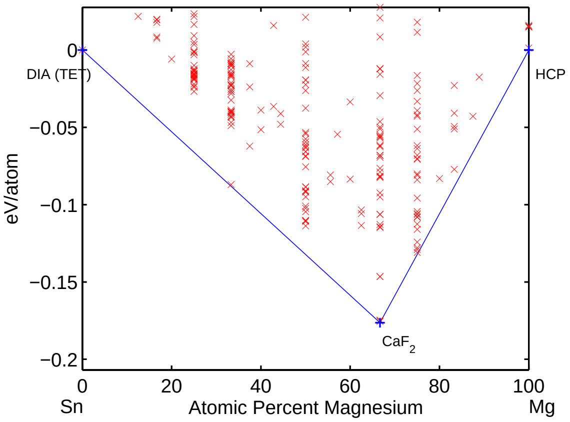

Figure 3.25 Mg-Sn convex hull. Ground states are labeled by the prototype and the Struckturbericht designation, if one exists.

Mg-Sr

Intermetallic compounds in the Mg-Sr system are only seen in the Mg-rich region. Experimental phases form at compositions Mg_2Sr, $Mg_{23}Sr_6$, $Mg_{38}Sr_9$, and $Mg_{17}Sr_2$. Ab initio ground states verify experimental phases.

Composition % Mg	Experimental results	Ab initio results
66.6	$MgZn_2$-C14	$MgZn_2$-C14 $MgNi_2$-C36 ∼1.9 meV/atom *above* C14
∼79.3	Th_6Mn_{23}	Th_6Mn_{23}
∼80.9	$Mg_{38}Sr_9$	***
∼89.5	Th_2Ni_{17}	Th_2Ni_{17}

Table 26 The Mg-Sr system. Experimental data taken from [33,209].

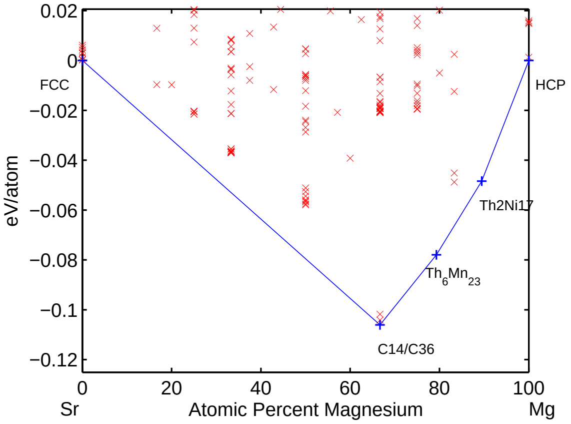

Figure 3.26 Mg-Sr convex hull. Ground states are labeled by the prototype and the Struckturbericht designation, if one exists.

Mg-Tc

To our knowledge, no published phase data exists for the sytem Mg-Tc. Ab initio compounds are predicted at compositions $MgTc_2$, Mg_3Tc_4, and MgTc.

Composition % Mg	Experimental results	Ab initio results
33.3	*non-compound forming*	$MoSi_2$-$C11_b$ ~15.8 meV/atom *below* $\Delta H = 0$
~42.9	*non-compound forming*	Cu_4Ti_3 ~20.2 meV/atom *below* $\Delta H = 0$
50.0	*non-compound forming*	CdTi ~22.4 meV/atom *below* $\Delta H = 0$

Table 27 The Mg-Tc system.

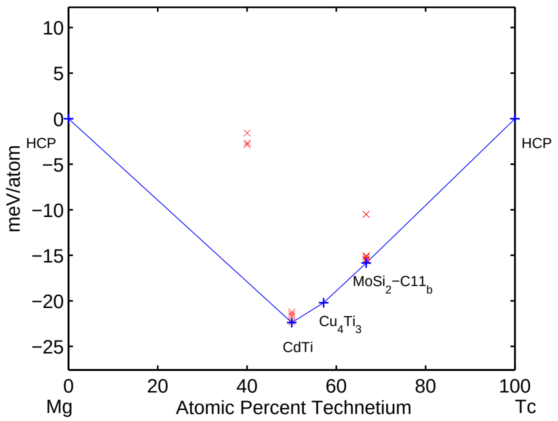

Figure 3.27 Mg-Tc convex hull. Ground states are labeled by the prototype and the Strukturbericht designation, if one exists.

Mg-Y

A rather surprising contradiction of the Mg-Y experimental phase diagrams exists in the ab initio data. The ground state at composition MgY_2 is the C49 ($ZrSi_2$) structure rather than the experimental phase C14 ($MgZn_2$). At T=0 K

C14 gives considerably higher formation enthalpy than the ab initio ground state even giving a positive value. The stability of the C14 phase at higher temperature may be due to finite temperature entropy effects (e.g, a phonon mode softening).

Composition % Mg	Experimental results	Ab initio results
33.3	$MgZn_2$-C14	Si_2Zr-C49 C14 ∼384.4 meV/atom *above* C49
50.0	CsCl-B2	CsCl-B2
75.0	*two-phase region*	$AlFe_3$-$D0_3$ Ni_3Sn-$D0_{19}$ ∼2.5 meV/atom *above* $D0_3$
∼82.8	$Re_{24}Ti_5$	*two-phase region* $Re_{24}Ti_5$ ∼3.8 meV/atom *above tie line*

Table 28 The Mg-Y system. Experimental data taken from [33, 210–216].

Mg-Zn

Ab initio data for the Mg-Zn system generally confirms low temperature phases reported in experimental phase diagrams. An unobserved Mg-rich phase is found, however, at composition Mg_2Zn, and there is no stable phase at composition MgZn (*unknown structure*). The CrB-B33 structure is closest to the tieline at this concentration (∼8.0 meV/atom above).

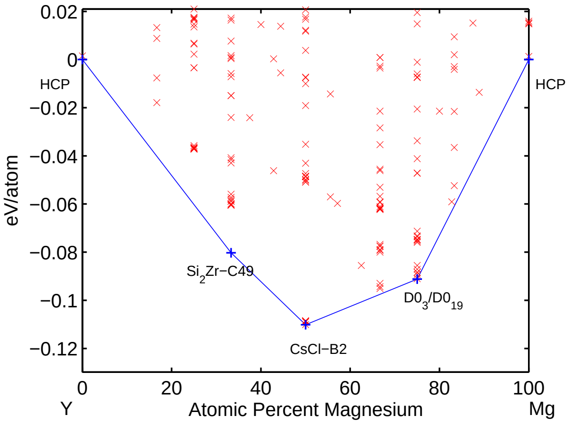

Figure 3.28 Mg-Y convex hull. Ground states are labeled by the prototype and the Struckturbericht designation, if one exists.

Composition % Mg	Experimental results	Ab initio results
∼15.3	Mg_2Zn_{11}	Mg_2Zn_{11}
33.3	$MgZn_2$-C14	$MgZn_2$-C14
∼36.3	Mg_4Zn_7	*two-phase region* Mg_4Zn_7 ∼11.8 meV/atom *above tie line*
50.0	MgZn *unknown*	*two-phase region* BCr-B33 ∼8.0 meV/atom *above tie line.*
66.6	*two-phase* *region*	Be_2Zn-65*

Table 29 The Mg-Zn system. Experimental data taken from [33,217–228].

Mg-Zr

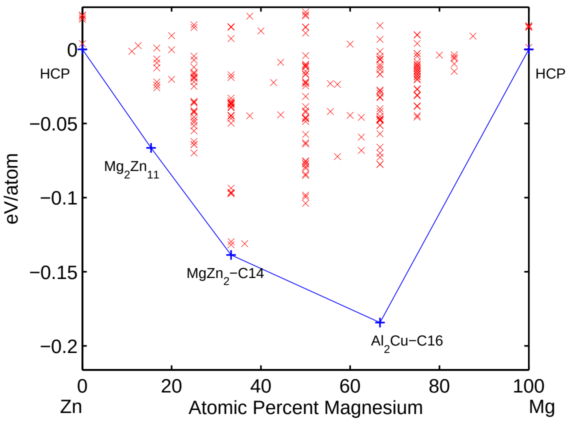

Figure 3.29 Mg-Zn convex hull. Ground states are labeled by the prototype and the Struckturbericht designation, if one exists.

Experimental phase diagrams show the Mg-Zr system to be non-compound forming. Two stable phases are predicted by ab initio calculations at compositions Mg_3Zr_4 and MgZr.

Composition % Mg	Experimental results	Ab initio results
∼42.9	*non-compound forming*	Cu_4Ti_3
50.0	*non-compound forming*	CdTi

Table 30 The Mg-Zr system. (†) See Structure Tables for crystallographic description. Experimental data taken from [33, 229, 230].

3.5 Conclusion

An extensive study was carried out on many binary magnesium systems: Using our HT framework AFLOW, we have explored the full composition ranges of

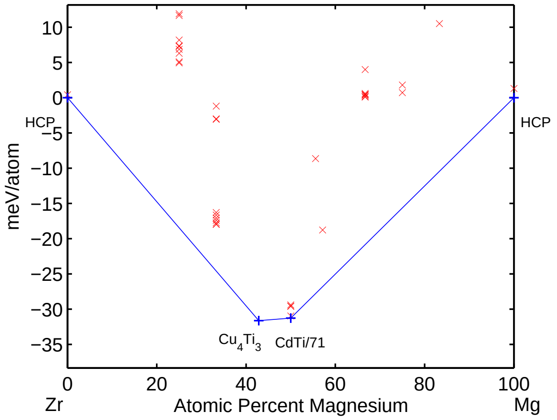

Figure 3.30 Mg-Zr convex hull. Ground states are labeled by the prototype and the Strukturbericht designation, if one exists.

39 Mg-X binary systems at $T = 0\,\mathrm{K}$. Nearly one third of the calculations are entirely consistent with published phase diagrams. That is, the ordered phases shown in the phase diagram coincide exactly with the low temperature ground state predictions of HT approach. In a little more two-thirds of cases, however, the differences between the DFT results and phase diagrams are noteworthy, suggesting new opportunities for alloy design.

On the level of individual phases, our study contrasts 71 experimental compounds with ab initio results. Of these 71, 12 were not evaluated with first principles due to either a large unit cell or undetermined structure. Ab initio data confirms 34 of 59 exactly–that is, 34 are found to be T=0 K ground states (∼60%). However, a simple evaluation of the data will reveal that many more are close in energy (∼10 meV) to tie lines, despite being too high to be included on the convex hull. At finite temperature (the regime of experiment) these phases are likely stabilized. When these additional phases are included 47 phases are found in agreement (∼80%).

The considerable agreement between ab initio predictions and experimental phases is encouraging. It should be emphasized also that the existence of contradictions does not necessarily indicate ab initio failure. Even so, if experimental phases with unknown structure, solid solution or two-phase regions, and the close-in-energy phases described above are excluded, direct contradiction occurs in only 6 systems (Table 31): Al-Mg, Ga-Mg, Ge-Mg, Mg-Pt, Mg-Si, and Mg-Y. Topological changes to the convex hull are predicted in even fewer systems (Al-Mg, Ga-Mg, Ge-Mg, Mg-Si) and are due exclusively to the Be_2Zn-65* phase. Systems believed to be phase-separating but for which negative ab initio enthalpies were obtained are listed in Table 32.

System	**Expected phase(s)**	**Ab initio phase(s)**
Al-Mg	$Al_{45}Mg_{28}/Al_{12}Mg_{17}$	$Al_2Mg/AlMg_2$-Be_2Zn-65*
Ga-Mg	$Mg_2Ga_5/MgGa_2/$ Mg_2Ga/Mg_5Ga_2	$Ga_2Mg/GaMg_2$-Be_2Zn-65*
Ge-Mg	CaF_2	$GeMg_2$-Be_2Zn-65*
Mg-Pt	FeSi-B20	AuCu-$L1_0$
Mg-Si	CaF_2	$Mg_2Si/MgSi_2$-Be_2Zn-65*
Mg-Y	$MgZn_2$-C14	Si_2Zr-C49

Table 31 Instances of direct contradiction of experimental results by ab initio calculations. Note that topological changes to the convex hull occur only when the Be_2Zn-65* phase is predicted.

System	Composition	Compound	Enthalpy (meV/atom)
Hf-Mg	HfMg	CdTi	-5.9
K-Mg	KMg_3	$73^\dagger$	-9.5
Mg-Na	Mg_3Na_2	Al_3Zr_2	-223.9
Mg-Rb	Mg_3Rb	$73^\dagger$	-396.2
Mg-Tc	$MgTc_2$	$MoSi_2$-$C11_b$	-15.8
	Mg_3Tc_4	Cu_4Ti_3	-20.2
	MgTc	CdTi	-22.4
Mg-Zr	Mg_3Zr_4	Cu_4Ti_3	-31.6
	MgZr	CdTi	-31.3

Table 32 Phase separating systems with ab initio compounds. (†) See Structure Tables for crystallographic description.

If one agrees, for the sake of argument, that ab initio data is correct even in instances of clear experimental disagreement, reasons for the discrepancies are not hard to imagine. Disagreement may certainly arise when experimental data is incomplete or shallow. Deficiencies in the experimental characterization of binary systems certainly exist due to the practical challenges associated with mixing alloys (e.g., reactivity, immiscibility, kinetics etc.) and finite-temperature entropy effects, but these are by no means exhaustive.

Whether it be the fault of ab initio calculations or experiment or neither, however, the largely aimless task of finding ordered phases by experiment alone is greatly focused by the data presented herein. The points of disagreement should be viewed as suggestions of further investigation, both theoretical and experimental as they offer the greatest potential for new alloy design.

Bibliography

[1] G. Shen and B. Duggan, Metall. Trans. A **38,** 2593 (2007).

[2] R. Jackson and P. Frost, "Properties and Current Applications of Magnesium-Lithium Alloys," NASA SP-5068 (1967).

[3] P. D. Frost, *Technical and Economic Status of Magnesium-Lithium Alloys* (1965).

[4] W. Counts, M. Friak, D. Raabe, and J. Neugebauer, "Using ab initio calculations in designing bcc Mg-Li alloys for ultra-lightweight applications," Acta Materialia **57,** 69–76 (2003).

[5] J. Catterall, Nature **169,** 336 (1952).

[6] G. Grube, H. Zeppelin, and H. Bumm, Z. Elektrochem. **40,** 160–164 (1934).

[7] P. Saldau and F. Schamray, "Gleichgewichtsdiagramm des Systems Magnesium-Lithium," Z. Anorg. Chem. **224,** 388–398 (1935).

[8] W. Freeth and G. Raynor, "The Systems Magnesium-Lithium and Magnesium-Lithium-Silver," J. Inst. Met. **82,** 575–580 (1953).

[9] W. Hume-Rothery, G. Raynor, and E. Butchers, J. Inst. Metals **71,** 589 (1945).

[10] W. Gasoir and Z. Moser, Metallurgical and Materials Transactions A **27,** 2419–2428 (1996).

[11] A. Nayeb-Hashemi, J. Clarck, and A. Pelton, "The Li-Mg (Lithium-Magnesium) System," Bulletin of Alloy Phase Diagrams **5,** 365–374 (1984).

[12] C. Barrett and O. Trautz, "Low-Temperature Transformations in Lithium and Lithium-Magnesium Alloys," Trans. Met. Soc. AIME **175,** 579–601 (1948).

[13] R. Berry and G. Raynor, Nature **171,** 1078–1079 (1953).

[14] F. Herbstein and B. Averbach, Acta Crystallogr. **9,** 91–92 (1956).

[15] S. Curtarolo, D. Morgan, and G. Ceder, "Accuracy of ab initio methods in predicting the crystal structures of metals: review of 80 binary alloys," Calphad **29,** 163 (2005).

[16] A. Nayeb-Hashemi, J. Clarck, and A. Pelton, *Binary Alloy Phase Diagrams*, 2 ed. (1990), Vol. 3, pp. 2444–2445.

[17] N. Saunders, "A Review and Thermodynamic Assessment of the Al-Mg and Mg-Li Systems," Calphad: Computer Coupling of Phase Diagrams and Thermochemistry **14,** 31–70 (1990).

[18] E. Schürmann and H. J. Voss, "Schmelzgleichgewichte des binären Systems Magnesium Lithium," Geissereiforschung **33,** 35–38 (1981).

[19] M. Saboungi and C. Hsu, "Computation of Isothermal Sections of the Al-Li-Mg System," Calphad: Computer Coupling of Phase Diagrams and Thermochemistry **1,** 237–251 (1977).

[20] O. Henry and H. Cordiano, "The Lithium-Magnesium Equilibrium Diagram," Transactions of the American Institute of Mining, Metallurgical and Petroleum Engineers **111,** 319–332 (1934).

[21] G. Kresse and J. Hafner, "Ab initio molecular dynamics for liquid metals," Phys. Rev. B 47 (1993).

[22] S. Froyen, "Brillouin-zone integration by Fourier quadrature: Special points for superlattice and supercell calculations," Phys. Rev. B **39,** 3168–3172 (1989).

[23] P. E. Blochl, "Projector augmented-wave method," Phys. Rev. B **50,** 17953 (1994).

[24] P. Blöchl, Phys. Rev. B **50,** 17953 (1994).

[25] S. Curtarolo, D. Morgan, K. Persson, J. Rodgers, and G. Ceder, "Predicting Crystal Structures with Data Mining of Quantum Calculations," Phys. Rev. Lett. **91,** 135503 (2003).

[26] D. Morgan, G. Ceder, and S. Curtarolo, Meas. Sci. Technolog. **16,** 296 (2005).

[27] O. Levy, G. L. W. Hart, and S. Curtarolo, "The new face of rhodium alloys: revealing ordered structures from first principles," submitted to Phys. Rev. Lett. (2009).

[28] S. Curtarolo, G. L. W. Hart, W. Setyawan, R. V. Chepulskii, O. Levy, and D. Morgan, *"AFLOW: software for high-throughput calculation of material properties"*, http://materials.duke.edu/aflow.html (2009).

[29] G. L. W. Hart and R. W. Forcade, "Generating derivative structures: Algorithm and applications," Phys. Rev. B **77,** 224115 (2008).

[30] G. L. W. Hart and R. W. Forcade, "Generating derivative structures from multilattices: Algorithm and application to hcp alloys," Physical Review B (Condensed Matter and Materials Physics) **80,** 014120 (2009).

[31] A. N. Kolmogorov and S. Curtarolo, "Theoretical study of metal borides stability," Phys. Rev. B **74,** 224507 (2006).

[32] P. Villars *et al.*, "The Pauling File, Binaries Edition," Journal of Alloys and Compounds **367,** 293–297 (2004).

[33] T. B. M. (Ed.), *Binary Alloy Phase Diagrams* (ASM International, Metals Park, OH, 1990).

[34] O. Levy, G. L. W. Hart, and S. Curtarolo, "Chasing exotic compounds: the necessary synergy of cluster expansion and high-throughput methods," submitted to Phys. Rev. Lett. (2009).

[35] J. Sanchez, F. Ducastelle, and D. Gratias, "Generalized Cluster Description of Multicomponent Systems," Physica A **128,** 334–350 (1984).

[36] G. L. W. Hart, V. Blum, M. J. Walorski, and A. Zunger, "Evolutionary Approach for Determination of First-Principles Hamiltonians," Nature Materials **4,** 391–394 (2005).

[37] V. Blum, G. L. W. Hart, M. J. Walorski, and A. Zunger, "Using genetic algorithms to map first-principles results to model Hamiltonians: Application to the generalized Ising model for alloys," Phys. Rev. B **72,** 165113 (2005).

[38] D. Lerch, O. Wieckhorst, G. L. W. Hart, R. W. Forcade, and S. Müller, "Constructing Cluster Expansions for Arbitrary Lattices from Minimal User Input," Model. Simul. Mater. Sci. Eng. (2009).

[39] A. van de Walle, M. Asta, and G. Ceder, "The alloy theoretic automated toolkit: A user guide," Calphad **26,** 539 – 553 (2002).

[40] A. van de Walle, "A complete representation of structure-property relationships in crystals," Nature Materials **7,** 455–458 (2009).

[41] Y. K. A. Seko and I. Tanaka, "Cluster expansion method for multicomponent systems based on optimal selection of structures for density-functional theory calculations," Physical Review B in press (2009).

[42] D. P. Landau and K. Binder, *A Guide to Monte Carlo Simulations in Statistical Physics* (Cambridge University Press, Cambridge, U.K., 2005).

[43] A. R. Harutyunyan, N. Awasthi, E. Mora, T. Tokune, A. Jiang, W. Setyawan, K. Bolton, and S. Curtarolo, "Reduced carbon solubility in Fe nano-clusters and implications for the growth of single-walled carbon nanotubes," Phys. Rev. Lett. **100,** 195502 (2008).

[44] S. Curtarolo, N. Awasthi, W. Setyawan, A. Jiang, K. Bolton, and A. R. Harutyunyan, "Influence of Mo on the Fe:Mo:C nano-catalyst thermo-

dynamics for single-walled carbon nanotube growth," Phys. Rev. B **78,** 054105 (2008).

[45] W. Kim, J. Zide, A. Gossard, D. Klenov, S. Stemmer, A. Shakouri, and A. Majumdar, "Thermal Conductivity Reduction and Thermoelectric Figure of Merit Increase by Embedding Nanoparticles in Crystalline Semiconductors," Phys. Rev. Lett. **96,** 045901 (2006).

[46] S. Wang and N. Mingo, "Improved thermoelectric properties of Mg[sub 2]Si[sub x]Ge[sub y]Sn[sub 1 - x - y] nanoparticle-in-alloy materials," Applied Physics Letters **94,** 203109 (2009).

[47] N. Mingo, D. Hauser, N. P. Kobayashi, M. Plissonnier, and A. Shakouri, ""Nanoparticle-in-Alloy" Approach to Efficient Thermoelectrics: Silicides in SiGe," Nano Lett. **9,** 711–715 (2009).

[48] R. W. Cahn, Metallurigcal Society Conference series 36 (1966).

[49] N. S. Stoloff and R. G. Davies, Prog. Mater. Sci. 13 (1966).

[50] M. Carelse and C. Lang, "Order hardening in platinum 14at.% copper," Scripta Materialia **54,** 1311–1315 (2006).

[51] A. Schneider and U. Z. Esch, Z. Electrochem. **50,** 290 (1944).

[52] D. Schryvers, J. V. Landuyt, and S. Amelinckx, Mater. Res. Bull. **18,** 1369–1374 (1983).

[53] Ni_8Nb is the prototype in some sources, although its discovery came some years after Pietrokowsky first reported Pt_8Ti.

[54] P. Pietrokowsky, "Novel Ordered Phase, Pt8Ti," Nature **206,** 291 (1965).

[55] P. Krautwasser, S. Bhan, and K. Schubert, Z. Metallkde. **59,** 724–729 (1968).

[56] W. E. Quist, C. van der Wekken, R. Taggart, and D. H. Polonis, Trans. Met. Soc. AIME **245,** 345–349 (1969).

[57] J. M. Larson, R. Taggart, and D. H. Polonis, Metall. Trans. **1,** 485–489 (1970).

[58] H. A. Moreen, R. Taggart, and D. H. Polonis, J. Mater. Sci. **6,** 1425–1432 (1971).

[59] L. Weaver and A. J. Ardell, Scripta Metall. **14,** 765–768 (1980).

[60] A. J. Ardell and K. Janghorban, *Phase Transitions During Irradiation* (Applied Sci. Pub., London, 1982), pp. 291–329.

[61] J. Mayer and K. Urban, Phys. Stat. Sol.(a) **90,** 469–475 (1985).

[62] M. S. Mostafa and A. J. Ardell, Mater. Lett. **3,** 67–70 (1987).

[63] M. P. Nzula, C. I. . Lang, and D. J. H. Cockayne, J. All. Comp. **420,** 165–170 (2006).

[64] Z. W. Lu and B. M. Klein, "Theoretical studies of the stability of ordered A8B compounds," Phys. Rev. B **50,** 5962–5970 (1994).

[65] D. Pettifor, "Structure maps for pseudobinary and ternary phases," Mater. Sci. Technol. **4,** 675 – 691 (1988).

[66] D. Pettifor, "Formation and stability of A8B phases in Ni, Pd, and Pt-base alloys," Met. Alloys: Exp. Theo. Persp. **256,** 93 – 102 (1994).

[67] G. L. W. Hart and R. Forcade, "Generating derivative structures from multilattices: Application to hcp alloys," Phys. Rev. B **80,** 014120 (2009).

[68] S. Curtarolo, D. Morgan, and G. Ceder, "Accuracy of ab initio methods in predicting the crystal structures of metals: review of 80 binary alloys," Calphad **29,** 163 (2005).

[69] O. Levy, G. L. W. Hart, and S. Curtarolo, "Uncovering Hafnium binary alloys from first principles," submitted to Phys. Rev. Lett. (2009).

[70] G. Kresse and J. Hafner, "Ab initio molecular dynamics for liquid metals," Phys. Rev. B **47,** 558 (1993).

[71] J. P. Perdew, K. Burke, and M. Ernzerhof, "Generalized gradient approximation made simple," Phys. Rev. Lett. **77,** 3865 (1996).

[72] A. N. Kolmogorov and S. Curtarolo, "Prediction of new crystal structure phases in metal borides: a lithium monoboride analog to MgB_2," Phys. Rev. B **73,** 180501(R) (2006).

[73] H. Zhang, S. Shang, J. Saal, A. Saengdeejing, Y. Wang, L.-Q. Chen, and Z.-K. Liu, "Enthalpies of formation of magnesium compounds from first-principles calculations," Intermetallics **17,** 878–885 (2009).

[74] S. Ganeshan, S. L. Shang, H. Zhang, Y. Wang, M. Mantina, and Z. K. Liu, "Elastic constants of binary Mg compounds from first-principles calculations," Intermetallics **17,** 313–318 (2009).

[75] V. E. Kolesnichenko, V. V. Karonik, S. N. Tsyganova, T. A. Kupriyanova, and L. N. Sysoeva, "Phase Equilibria in the ϵ-phase region of the Mg-Ag system," Russian Metallurgy, translated from Izvestiya Akademii Nauk SSSR **5,** 188–192 (1988).

[76] E. Schürmann and R. Engel, "Untersuchung der Phasengleichgewichte magnesiumreicher . . .," Giessereiforschung **38,** 58–66 (1986).

[77] G. V. Raynor, B. R. T. Frost, and W. H. Hall, "The system silver-magnesium-tin, with referenece to the theory of ternary alloys," Journal of the Institute of Metals **75,** 778–808 (1948 and 49).

[78] K. W. Andrews and W. H. Rothery, Journal of the Institute of Metals **69,** 485–493 (1943).

[79] H. Nishimura and H. Sawamoto, Suiyokwai-Shi (Transactions of the Mining and Metallurgical Association, Kyoto) **9,** 645–654 (1938).

[80] R. J. M. Payne and J. L. Haughton, Journal of the Institute of Metals **60,** 351–364 (1937).

[81] W. H. Rothery and E. Butchers, Journal of the Institute of Metals **60,** 345–350 (1937).

[82] N. Parravano, Gazzetta Chimica Italiana **38,** 167–186 (1908).

[83] S. F. Zemozuzny, Zetischrift für Anorganische Chemie **49,** 400–414 (1906).

[84] Y. Zuo and Y. Chang, "Thermodynamic calculation of the Al-Mg phase diagram," Calphad: Computer Coupling of Phase Diagrams and Thermochemistry **17,** 161–174 (1993).

[85] N. Saunders, "A Review and Thermodynamic Assessment of the Al-Mg and Mg-Li systems," Calphad: Computer Coupling of Phase Diagrams and Thermochemistry **14,** 61–70 (1990).

[86] E. Schürmann and R. Engel, "Untersuchung der Phasengleichgewichte . . .," Giessereiforschung **38,** 58–66 (1986).

[87] Y. Minamino, T. Yamane, T. Miyake, M. Koizumi, and Y. Miyamoto, "Effect of high pressure on diffusion reactions and phase diagrams in Al-Mg system," Materials Science and Technology **2,** 777–783 (1986).

[88] H. J. Voss and E. Schürmann, "Untersuchung der Schmelzgleichgewichte von Magnesium-Lithium-Aluminium-Legierungen," Giessereiforschung **33,** 43–46 (1981).

[89] E. Schürmann and I. K. Geissler, "Teil 3. Phasengleichgewichte des festen Zustandes im System Aluminium-Magnesium," Giessereiforschung **32,** 167–170 (1980).

[90] M. L. Saboungi and C. C. Hsu, "Computation of isothermal sections of the Al-Li-Mg system," Calphad: Computer Coupling of Phase Diagrams and Thermochemistry **1,** 237–251 (1977).

[91] E. Schürmann and A. Fischer, "Schmelzgleichgewichte im Dreistoffsystem Aluminum-Magnesium-Silicium: Teil 1 Zweistoffsystem Aluminum-Magnesium," Giessereiforschung **29,** 107–111 (1977).

[92] W. Wachtel, S. Woerner, and S. Steeb, "Magnetische Eigenschaften von Aluminium-Magnesium-Legierungen im festen und geschmolzenen Zustand," Zeitschrift für Metallkunde **56,** 776–778 (1965).

[93] K. A. Bolshakov, P. I. Fedorov, and E. I. Smarina, "β phase of the aluminium-magnesium system," Russian Journal of Inorganic Chemisty, translated from Zhurnal Neorganicheskoi Khimii **8,** 734–738 (1963).

[94] J. B. Clark and F. N. Rhines, "Aluminium-Magnesium Equilibrium Diagram," Transactions of the American Institute of Mining, Metallurgical and Petroleum Engineers **209,** 6–7 (1957).

[95] K. Übersicht, K. Eickhoff, and H. Vosskühler, "Das Zustandsbild des Systems Aluminium-Magnesium," Zeitschrift für Metallkunde **44,** 223–231 (1953).

[96] M. I. Zakharova and V. A. Il'ina, "Change of the range of the solid solution at compression under pressure in the systems Al-Mg and Al-Ag," Zhurnal Fizicheskoi Khimii **24,** 714–717 (1950).

[97] K. Little, H. J. Axon, and W. Hume-Rothery, "The constitution of aluminium-magnesium-zinc-chromium alloys at 460°C," Journal of the institute of metals 75 (1948).

[98] E. Butchers and W. Hume-Rothery, "On the constitution of aluminium-magnesium-manganese-zinc alloys: the solidus," Journal of the institute of metals **71,** 291–311 (1945).

[99] W. Köster and E. Wagner, "Der Teilbereich Mg-Al3Mg4-Mg5Tl2 des Dreistoffsystems Magnesium-Aluminium-Thallium," Zeitschrift für Metallkunde **30,** 338–342 (1938).

[100] W. Hume-Rothery and G. V. Raynor, "The constitution of the magnesium-rich alloys in the systems aluminium-magnesium, gallium-

magnesium, indium-magnesium, and thallium-magnesium," Journal of the Institute of Metals **63,** 201–226 (1938).

[101] W. L. Fink and L. A. Willey, "Equilibrium Relations in the Aluminium-magnesium-zinc alloys of high purity," Transactions of the American Institute of Mining, Metallurigical and Petroleum Engineers **124,** 78–110 (1937).

[102] C. Goria and G. Venturello, "Reattivita di leghe binarie: Note I," Gazzetta Chimica Italiana **67,** 487–501 (1937).

[103] J. L. Haughton and R. J. M. Payne, Journal of the Institute of Metals **57,** 287–296 (1935).

[104] P. Saldau and M. Zamotorin, Journal of the Institute of Metals **48,** 221–226 (1932).

[105] G. Siebel and E. Schmid, Zeitschrift für Metallkunde **23,** 202–202 (1931).

[106] D. Hanson and M. L. V. Gayler, Journal of the Institute of Metals **26,** 321–359 (1921).

[107] D. Hanson and M. L. V. Gayler, Journal of the Institute of Metals **24,** 201–232 (1920).

[108] R. Vogel, Angewandte Chemie **35,** 705–708 (1922).

[109] G. G. Urasow, Zeitschrift für Anorganische Chemie **64,** 375–396 (1909).

[110] R. Vogel, Zeitschrift für Anorganische Chemie **63,** 169–183 (1909).

[111] A. Renu, L. J. Joong, H. L. Lukas, and F. Sommer, Zeitschrift für Metallkunde **86,** 103–108 (1995).

[112] W. Klemm and F. Dinkelacker, Zeitschrift für Anorganische Chemie **255,** 2–12 (1947).

[113] W. Bulian and E. Fahrenhorst, Zeitschrift für Metallkunde **37,** 70 (1946).

[114] H. Nowotny, E. Wormnes, and A. Mohrnheim, Zeitschrift für Metallkunde **32,** 39–42 (1940).

[115] H. Vosskühler, Zeitschrift für Metallkunde **29,** 236–237 (1937).

[116] J. L. Haughton, Journal of the Institute of Metals **61,** 241–246 (1937).

[117] N. Baar, Zeitschrift für Anorganische Chemie **70,** 352–394 (1911).

[118] M. Asta, R. McCormack, and D. D. Fontaine, Physical Review B: Condensed Matter **48,** 748–766 (1993).

[119] M. Asta, R. McCormack, and D. D. Fontaine, Giessereiforschung **36,** 53–59 (1984).

[120] R. Castanet, Z. Moser, and W. Gasior, Calphad: Computer Coupling of Phase Diagrams and Thermochemistry **4,** 231–239 (1980).

[121] G. Fischer, D. Godel, and S. Steeb, Zeitschrift für Metallkunde **64,** 200–203 (1973).

[122] P. C. Frantz and M. Gantois, Journal of Applied Crystallography **4,** 387–395 (1971).

[123] C. Frantz, M. Gantois, and A. Pianelli, Comptes Rendus Hebdomandaires des Seances de lÁcademie des Sciences **265,** 1019–1022 (1967).

[124] S. B. Felgina, Russian Metallurgy and Mining **6,** 96–99 (1964).

[125] O. Kubaschewski and T. G. Chart, Journal of the Institute of Metals 93 (1964).

[126] J. B. Newkirk, Transactions of the American Institute of Mining, Metallurgical and Petroleum Engineers **200,** 673–675 (1954).

[127] W. Hume-Rothery and G. V. Raynor, Proceedings of the Royal Society of London **174,** 471–486 (1940).

[128] W. Köster and E. Wagner, Zeitschrift für Metallkunde **30,** 335–338 (1938).

[129] E. Jünecke, Zeitschrift für Metallkunde **30,** 424–429 (1938).

[130] G. Grube and E. Schiedt, Zeitschrift für Anorganische und Allgemeine Chemie **194,** 190–222 (1930).

[131] W. H. Rothery and S. W. Rowell, Journal of the Institute of Metals **38,** 137–156 (1927).

[132] G. Bruni and C. Sandonnini, Zeitschrift für Anorganische Chemie **78,** 273–297 (1912).

[133] G. Grube, Zeitschrift für Anorganische Chemie **49,** 72–92 (1906).

[134] Y. Zuo and Y. A. Chang, Zeitschrift für Metallkunde **84,** 662–667 (1993).

[135] C. A. Coughanowr, I. Ansara, R. Luoma, M. Hamalainen, and H. L. Lukas, Zeitschrift für Metallkunde **82,** 574–581 (1991).

[136] P. Bagnoud and P. Feschotte, Zeitschrift für Metallkunde **69,** 114–120 (1978).

[137] W. R. D. Jones, Journal of the Institute of Metals **46,** 395–422 (1931).

[138] O. Dahl, Wissenschaftliche Veröffentlichungen aus den Siemens Werken **6,** 222–234 (1927).

[139] O. Levy, G. Hart, and S. Curtarolo, "Structure maps for hcp metals from first principles calculations," Phys. Rev. B **81,** 174106 (2010).

[140] M. Notin, E. Belbacha, J. Charles, and J. Hertz, "New experimental results and improvement of the modelization of the (Ga,Mg) system," Journal of Alloys and Compounds **176,** 25–38 (1991).

[141] M. Ellner, T. Gödecke, G. Duddek, and B. Predel, Zeitschrift für Anaorganische und Allgemeine Chemie **463,** 170–178 (1980).

[142] B. Predel and D. W. Stein, Journal of the Less-Common Metals **18,** 203–213 (1969).

[143] W. H. Rothery and G. V. Raynor, Journal of the Institute of Metals **63,** 201–226 (1938).

[144] N. A. Pusin and O. D. Micic, Zeitschrift für Anaorganische und Allgemeine Chemie **234,** 229–232 (1937).

[145] Y. K. Rao and G. R. Belton, Metallurgical Transactions **2,** 2215–2219 (1971).

[146] R. Geffken and E. Miller, Transactions of the Metallurgical Society of AIME **242,** 2323–2328 (1968).

[147] H. Westlinning and W. Klemm, Zeitschrift für Anaorganische und Allgemeine Chemie **245,** 365–380 (1941).

[148] G. V. Raynor, Journal of the Institute of Metals **66,** 403–426 (1940).

[149] O. Levy, G. L. W. Hart, and S. Curtarolo, “Hafnium binary alloys from experiments and first principles,” Acta Materialia **58,** 2887–2897 (2010).

[150] F. A. Calvo and M. P. Hierro, Revista de Metalurgia (Madrid) **23,** 333–340 (1987).

[151] W. Klemm, **62,** 133–142 (1950).

[152] H. Nowotny, Zeitschrift für Metallkunde **37,** 130–136 (1946).

[153] P. Feschotte, Journal of the Less-Common Metals **46,** 51–54 (1976).

[154] Y. Watanabe, Acta Metallurgica **23,** 691–696 (1975).

[155] K. M. Pickwick, W. A. Alexander, and R. H. Gamble, Canadian Journal of Chemistry **47,** 3417–3427 (1969).

[156] M. Hirabayashi, M. Koiwa, and K. Hiraga, Journal of the Less-Common Metals **15,** 109–119 (1968).

[157] N. Ino, M. Hirabayashi, and S. Ogawa, Transactions of the Japan Institute of Metals **6,** 172–178 (1965).

[158] G. V. Raynor and J. Graham, Philosophical Magazine **2,** 1354–1363 (1957).

[159] W. H. Rothery and G. V. Raynor, Journal of the Institute of Metals **63,** 201–226 (1938).

[160] L. Hunt, “A History of Iridium: OVERCOMING THE DIFFICULTIES OF MELTING AND FABRICATION,” Platinum Metlas Review **31,** 32–41 (1987).

[161] R. Ferro, G. Rambaldi, and R. Capelli, Journal of the Less-Common Metals **4,** 16–23 (1962).

[162] A. D. Pelton, Bulletin of Alloy Phase Diagrams **6,** 39–41 (1985).

[163] R. M. R. F. M. Giovannini, A Saccone, Metallurgical Transactions, Section A: Physical Metallurgy and Materials Science **26,** 5–10 (1995).

[164] K. J. G. P. Manfrinetti, Journal of the Less-Common Metals **123,** 267–275 (1986).

[165] K. J. G. R.R. Joseph, Transactions of the Metallurgical Society of AIME **233,** 2063–2069 (1965).

[166] S. Felgina, Russian Metallurgy and Mining **6,** 96–99 (1964).

[167] R. Vogel and T. Heumann, Zeitschrift für Metallkunde **38,** 1–8 (1947).

[168] F. Weibke and W. Schmidt, Zeitschrift für Elektrochemie und Angewandte Physikalische Chemie **46,** 357–364 (1940).

[169] R. H. Taylor, S. Curtarolo, and G. L. W. Hart, "Ordered magnesium-lithium alloys: First-principles predictions," Phys. Rev. B **81,** 024112 (2010).

[170] N. Saunders, Calphad: Computer Coupling of Phase Diagrams and Thermochemistry **14,** 61–70 (1990).

[171] E. Schürmann and H. J. Voss, Giessereiforschung **33,** 35–38 (1981).

[172] E. Schürmann and I. K. Geissler, Giessereiforschung **32,** 165–167 (1980).

[173] M. L. Saboungi and C. C. Hsu, Calphad: Computer Coupling of Phase Diagrams and Thermochemistry **1,** 237–251 (1977).

[174] W. E. Freeth and G. V. Raynor, Journal of the Institute of Metals 82 (1953).

[175] J. A. Caterall, Nature (London) **169,** 336– (1952).

[176] W. H. Rothery, G. V. Raynor, and E. Butchers, Journal of the Institute of Metals **71,** 589–601 (1945).

[177] W. Hofmann, Zeitschrift für Metallkunde **28,** 160–163 (1936).

[178] P. Saldau and F. Schamray, Zeitschrift für Anorganische und Allgemeine Chemie **224,** 388–398 (1935).

[179] O. H. Henry and H. V. Cordiano, Transactions of the American Institute of Mining, Metallurgical and Petroleum Engineers **111,** 319–332 (1934).

[180] C. D. G. Jr., J. A. Burgo, J. W. Cooper, C. L. Douglas, P. S. Gilman, W. T. Kelley, and A. Nagelberg, Metallurgical Transactions **2,** 2964–2965 (1971).

[181] J. M. Eldridge, E. Miller, and K. L. Komarek, Transactions of the Metallurgical Society of AIME **233,** 1303–1308 (1965).

[182] G. W. Horsley and J. T. Maskrey, Journal of the Institute of Metals 86 (1957).

[183] F. Foote and E. R. Jette, Petroleum Engineers **143,** 124–133 (1941).

[184] G. V. Raynor, Journal of the Institute of Metals **66,** 403–426 (1940).

[185] H. Vosskühler, Zeitschrift für Metallkunde **31,** 109–111 (1939).

[186] J. Goebel, Zeitschrift für Metallkunde **14,** 357–366 (1922).

[187] N. S. Kurnakow and N. J. Stepanow, Zeitschrift für Anorganische Chemie **46,** 177–192 (1905).

[188] E. M. Savitskii, V. F. Terekhova, and N. A. Birun, Russian Journal of Inorganic Chemistry **7,** 1228–1231 (1962).

[189] W. Bronger and W. Klemm, “Preparation of Alloys of Platinum with Non-Noble Metals,” Zeitschrift für anorganische und allgemeine Chemie **319,** 58–81 (1962).

[190] B. J. Beaudry and A. H. Daane, Journal of the Less-Common Metals **18,** 305–308 (1969).

[191] D. Lüdecke, Zeitschrift für Metallkunde **77,** 278–287 (1986).

[192] P. Dörner, H. Kreig, H. L. Lukas, R. Müller, and G. Petzow, Calphad: Computer Coupling of Phase Diagrams and Thermochemistry **5,** 41–54 (1981).

[193] E. Schürmann and A. Fischer, Giessereiforschung **29,** 111–113 (1977).

[194] R. Geffken and E. Miller, Transactions of the Metallurgical Society of AIME **242,** 2323–2328 (1968).

[195] G. V. Raynor, Journal of the Institute of Metals **66,** 403–426 (1940).

[196] B. E. H. Sawamoto, Suiyokwai-Shi (Transactions of the Mining and Metallurgical Association Kyoto) **8,** 713–728 (1935).

[197] R. Vogel, Zeitschrift für Anorganische Chemie **61,** 46–53 (1909).

[198] S. Srinivasan, Zeitschrift für Metallkunde **82,** 841–845 (1991).

[199] B. Jönsson and J. A. gren, Metallurgical Transactions, Section A: Physical Metallurgy and Materials Science **17,** 607–615 (1986).

[200] L. M. Pavlova and K. B. Poyarkov, Russian Journal of Physical Chemistry **56,** 183–185 (1982).

[201] A. K. Nayak and W. Oelsen, Transactions of the Indian Institute of Metals **21,** 15–20 (1968).

[202] J. M. Eldridge, E. Miller, and K. L. Komarek, Transactions of the Metallurgical Society of AIME **236,** 114–121 (1966).

[203] S. B. Felgina, Russian Metallurgy and Mining **6,** 96–99 (1964).

[204] W. Wobst, Zeitschrift für Physikalische Chemie, Abteilung B **219,** 239–265 (1962).

[205] G. V. Raynor, Journal of the Institute of Metals **66,** 403–426 (1940).

[206] W. H. Rothery, Journal of the Institute of Metals **35,** 295–361 (1926).

[207] W. H. Rothery, Zeitschrift für Anorganische Chemie **46,** 177–192 (1905).

[208] G. Grube, Zeitschrift für Anorganische Chemie **46,** 76–93 (1905).

[209] W. Klemm and F. Dinkelacker, Zeitschrift für Anorganische Chemie **255,** 2–12 (1947).

[210] Q. Ran, H. L. Lukas, G. Effenberg, and G. Petzow, Calphad: Computer Coupling of Phase Diagrams and Thermochemistry **12,** 375–381 (1988).

[211] Z. A. Sviderskaya and E. M. Padezhnova, Russian Metallurgy **6,** 126–130 (1988).

[212] D. Miannay, P. Grégoire, P. Azou, and P. Bastien, Comptes Rendus Hebdomadaires des Seances de l'Academie des Sciences, Serie C: Sciences Chimiques **265,** 1107–1112 (1967).

[213] J. F. Smith, D. M. Bailey, D. B. Novotny, and J. E. Davison, Acta Metallurgica **13,** 889–895 (1965).

[214] I. L. Markova, V. F. Terekhova, and E. M. Savitskii, Voprosy Teorii i Primeneniya Redkozemel ńykh Metallov .

[215] D. Mizer and J. B. Clark, Transactions of the American Institute of Mining, Metallurgical and Petroleum Engineers **221,** 207–208 (1961).

[216] E. D. Gibson and O. N. Carlson, Transactions of the American Society for Metals **52,** 1084–1096 (1960).

[217] T. Gödecke and F. Sommer, Zeitschrift für Metallkunde **85,** 683–691 (1994).

[218] R. Agarwal, S. G. Fries, H. L. Lukas, G. Petzow, F. Sommer, T. G. Chart, and G. Effenberg, Zeitschrift für Metallkunde **83,** 216–223 (1992).

[219] M. E. Drits, Z. A. Sviderskaya, E. S. Kadaner, and S. B. Felgina, Russian Metallurgy and Mining **5,** 90–97 (1963).

[220] K. P. Adnerko, E. J. Klimek, D. W. Levinson, and W. Rostoker, Transactions of the American Society of Metals **49,** 778–793 (1957).

[221] J. B. Clark and F. N. Rhines, Transactions of the American Institute of Mining, Metallurgical and Petroleum Engineers **209,** 425–430 (1957).

[222] W. Klemm, Angewandte Chemie **62,** 133–142 (1950).

[223] F. Laves, Naturwissenschaften **27,** 454–455 (1939).

[224] W. H. Rothery and E. O. Rounsefell, Journal of the Institute of Metals **41,** 119–138 (1929).

[225] R. Chadwick, Journal of the Institute of Metals **39,** 285–300 (1928).

[226] G. Bruni and C. Sandonnini, Zeitschrift für Anorganische Chemie **78,** 273–297 (1912).

[227] I. Mitteilung, G. Bruni, C. Sandonnini, and E. Quercigh, Zeitschrift für Anorganische Chemie **68,** 73–90 (1910).

[228] G. Grube, Zeitschrift für Anorganische Chemie **49,** 72–92 (1906).

[229] G. A. Mellor, Journal of Institute of Metals **77,** 163–174 (1950).

[230] F. Sauerwald, Zeitschrift für Anorganische Chemie **255,** 212–220 (1947).

Appendix A

Cluster expansion methods

The genetic algorithm and *leave one out cross validation* provide a useful framework for constructing a CE that accurately fits input data; furthermore, a CE produced in this manner is capable of predicting the energy of structures not included in the input set provided that the 'physics' of the input data is representative of the entire system (although off-lattice structures are not included in the configuration space, HT and experimental data suggest that additional structures will not form in Mg-Li: Not only are the HT energies higher than both HCP and bcc CE predicted structure energies, but the majority of HT ground state predictions are bcc superstructures.)

By adding structures in under-fit regions to the input structure set, the overall predictive capacity of the CE was improved. Low energy structures without similar input structures as well as additional structures similar in configuration to poorly predicted input structures were added to the input set. Structures were added in this manner by comparing successive fits, so that the final input data set was determined to ensure a broadly accurate parameterization of configuration space [36]. A total of 85 bcc and 71 hcp derived superstructures were ultimately used in the construction of the CEs.

The utility of the iterative process hints at the underlying physical workings of the CE method. Input structures contribute to the CE via the addition of ‘physics’ yet unaccounted for. Iteratively adding structures from regions of poorly fit data, and from regions lacking input data, will then in principle lead to a CE capable of making accurate predictions across configuration space. Furthermore, given a set if interaction terms representative of the system, the inclusion of additional input data should do little to alter the ground state predictions of the CE constructed using these figures.

The *durability* of the fit, i.e., the immutability of ground state predictions with the inclusion of new input data, was studied in the following manner. A database containing the complete set of input structures was parsed into input sets of increasing size; this was done several times with unique parsing, and a CE was constructed for each input set. Ground state predictions made by the CEs were compared for agreement, and frequently predicted ground state concentrations formed a group of credible predictions.

For bcc Mg-Li, a database containing the formation enthalpies of 85 input structures were parsed into 39 groups of input structures 5 times. CEs were constructed for each of the 39 groups yielding 39 predictions of the Mg-Li ground states. The structures and associated concentrations predicted by fits containing the entirety of the input data (A-E) are listed in Table 1. The frequencies of prediction of ground states at each listed concentration are shown in the second column. It is seen that the predictions made by CEs constructed using the entire input set generally correspond to predictions made by the majority of fits.

The hcp Mg-Li system was treated similarly. Input data computed for 71 input structures was parsed into 33 unique input sets 5 times. In contrast to the bcc case, however, several concentrations not predicted by CEs constructed using the complete input data were found to have a high frequency of prediction by the totality of fits. Thus, these are also included in the table (Table 2).

The potential ground state pool was significantly reduced by comparing the predictions of many CEs. However, because the precision necessary to distinguish small differences in structure energetics are not to be expected from the finite CE, DFT was used to directly compare the energies of the final group of candidates. VASP was used to evaluate each of the candidate structures listed in Tables 1 and 2 as well as candidate structures not necessarily predicted by fits A-E but with significant frequency of occurrence.

x (Mg)	#/195 (%)	A	B	C	D	E
1/8	24	631	631			
2/9	11	1134		1134		1134
1/3	66	10	125	10	10	10
3/8	27					404
2/5	59	45	45	45	45	48
4/9	21	938				
1/2	97	19	19	19	19	19
4/7	27			191	191	
2/3	92	7	7	7	7	7
3/4	70	277	277	277	277	277
7/9	32		1112		1112	
4/5	70	54		54		54
5/6	18		62			
7/8	52		593	593	593	436
8/9	63	1052				
9/10	31		1145	1142		2309

Table 1 Columns A-E contain the predicted structures (numbered in accordance with the enumeration algorithm) from five 85-input generated fits for bcc Mg-Li. The percentage occurrence of ground states to the total number of fits (195) is given in the second column. Except for 9/10 and 2/9 percent Mg ground states, the predictions in A-E affirm the ground state predictions made by the majority of total fits (195).

x (Mg)	#/165 (%)	A	B	C	D	E
1/8	33	333		333	318	333
1/7	36					
1/6	72	3920	3920	3920	3920	3920
1/4	83					
1/3	37					
1/2	100	12	12	12		12
2/3	64					
3/4	61	321	321	321		303
4/5	30					
5/6	82	1491	1491	1491	1491	1491
6/7	38					
7/8	18		319			

Table 2 Hcp Mg-Li ground state predictions as in Table 1. Several frequent predictions are not affirmed by full fits, and thus additional concentrations have been included.

Appendix B

Structure tables

Table 1 Crystallographic information for less-familiar prototypes arising in our study from [29,139,149]. Atomic positions and unit cell parameters are fully relaxed (indicated by '*'). Corresponding unrelaxed structures are given in 3.

Compound	Be$_2$Zn-65*	Hf$_5$Pb-f63*	Hf$_2$Tl-6*
Lattice	Orthorhombic	Tetragonal	Tetragonal
Space group	Fmmm #69	P4/mmm #123	I4/mmm #139
Pearson symbol	oF12	tP6	tI6
Primitive vect.	(SG option 2)	—	(SG option 2)
(a,b,c) (Å)	(3.780, 2.0978, 10.3)	(3.203,3.203,13.944)	(4.422,4.422,7.385)
(α,β,γ) (deg)	(90,90,90)	(90,90,90)	(90,72.577,90)
Wyckoff	(0,0,0.17832) 8i Be1	(0,0,-0.1794) 2g Hf1	(0,0,0.1746) 4e Hf1
positions	$(0,0,\frac{1}{2})$ 4b Zn1	$(\frac{1}{2},\frac{1}{2},-0.3349)$ 2h Hf2	$(0,0,\frac{1}{2})$ 2b Tl2
	—	$(0,0,\frac{1}{2})$ 1b Hf3	—
	—	$(\frac{1}{2},\frac{1}{2},0)$ 1c Pb1	—
AFLOW label	"549"	"477"	"547"
Compound	HfPd$_5$-f137*	Re$_3$Ru-124*	Mo$_3$Ti-81*
Lattice	Orthorhombic	Orthorhombic	Orthorhombic
Space group	Cmmm #65	Imm2 #44	Immm #71
Pearson symbol	oS12	oI8	oI8
Primitive vect.	(11.998,4.0663,14.0723)	(9.005, 2.757, 4.775)	(4.444,3.173,8.971)
	(90,90,90)	(90,90,90)	(90,90,90)
Wyckoff	(0,0,0) 2a Hf1	$(\frac{1}{4},0,0)$ 4c Re1	(0,0,0.2440) 4i Mo1
positions	$(0.1663,0,\frac{1}{2})$ 4h Pd1	$(0,\frac{1}{2},\frac{1}{6})$ 2b Re2	$(0,\frac{1}{2},0)$ 2d Mo2
	(0.3369,0,0) 4g Pd2	$(0,0,\frac{2}{3})$ 2a Ru1	$(\frac{1}{2},0,0)$ 2b Ti1
	$(\frac{1}{2},0,\frac{1}{2})$ 2c Pd3	—	—
AFLOW label	"479"	"551"	"541"

Table 2 Crystallographic data for unrelaxed prototypes reported in Table 1.

Compound	Be_2Zn	Hf_5Pb	Hf_2Tl
Superlattice	bcc	fcc	fcc
Lattice	Orthorhombic	Tetragonal	Tetragonal
Space group	Fmmm #69	P4/mmm #123	I4/mmm#139
Pearson symbol	oF12	tP6	tI6
Primitive vect.			
$\mathbf{a}_1$/a	(0,1,2)	(1/2,1/2,0)	(3/2,0,-1/2)
$\mathbf{a}_2$/a	(-1/2,3/2,3/2)	(0,3,3)	(3/2,0,1/2)
$\mathbf{a}_3$/a	(-1/2,-1/2,1/2)	(1/2,5/2,3)	(-3/2,-1/2,0)
Atomic Positions			
A1	(0,0,0)	(0,0,0)	(2/3,2/3,0)
A2	(2/3,2/3,1/2)	(0,1/6,0)	(1/3,1/3,0)
A3	—	(0,1/3,0)	—
A4	—	(0,1/2,0)	—
A5	—	(0,2/3,0)	—
B1	(1/3,1/3,2/3)	(0,5/6,0)	(0,0,0)
AFLOW label	“65”	“f63”	“6”

Table 3 Additional crystallographic data for unrelaxed prototypes reported in Table 1.

Compound	Mo_3Ti	$HfPd_5$	Re_3Ru
Superlattice	bcc	hcp	hcp
Lattice	Orthorhombic	Orthorhombic	Orthorhombic
Space group	Immm #71	Cmmm #65	Imm2 #44
Pearson symbol	oI8	oS12	oI8
Primitive vect.			
$\mathbf{a}_1$/a	(3/2,1/2,-1/2)	(1/2,3/2,1)	$(1/2,-\sqrt{2}/3,1.633)$
$\mathbf{a}_2$/a	(1/2,3/2,1/2)	(0,3,3)	$(-1/2,\sqrt{2}/3,1.633)$
$\mathbf{a}_3$/a	(-1/2,-3/2,1/2)	(1/2,3/2,2)	$(-1/2,-\sqrt{2}/3,-1.633)$
Atomic Positions			
A1	(0,0,0)	(0,0,0)	(0,0,0)
A2	(1/4,3/4,1/2)	(0,1/6,0)-B1	(1/2,1/2,0)
A3	(1/2,1/2,0)	(0,1/3,0)-B2	(1/12,3/4,1/3)
A4	—	(0,1/2,0)-B	— 3
A5	—	(0,2/3,0)-B4	—
B1	(3/4,1/4,1/2)	(0,5/6,0)-B5	(7/12,1/4,1/3)
AFLOW label	“81”	“f137”	“124”

Table 4 Crystallographic data for other unrelaxed bcc-, fcc-, hcp-derived prototypes arising in our study.

Compound	AB_4	AB_3	A_2B_2
Superlattice	fcc	bcc	bcc
Lattice	Monoclinic	Monoclinic	Orthorhombic
Space group	C2/m #12	P2/m #10	Cmma #67
Pearson symbol	mS10	mP4	oS8
Primitive vect.			
$\mathbf{a}_1/a$	(1/2,1/2,0)	(0,-2,0)	(1/2,1/2,1/2)
$\mathbf{a}_2/a$	(0,5/2,5/2)	(-1,0,-1)	(-1/2,-1/2,1/2)
$\mathbf{a}_3/a$	(1/2,1,3/2)	(1/2,5/2,-1/2)	(2,-2,0)
Atomic Positions			
A1	(0,0,0)	(0,0,0)	(0,0,0)
A2	—	—	(1/2,1/2,3/4)
B1	(0,1/5,0)	(3/4,1/2,0)	(0,1/2,1/4)
B2	(0,2/5,0)	(1/2,0,0)	(1/2,1/2,1/4)
B3	(0,3/5,0)	(1/4,1/2,0)	—
B4	(0,4/5,0)	—	—
AFLOW label	"f_{52}"	"73"	"71"

Table 5 Additional crystallographic data for other unrelaxed bcc-, fcc-, hcp-derived prototypes arising in our study.

Compound	A_2B_2	A_2B_2	A_2B_2
Superlattice	fcc	fcc	bcc
Lattice	Monoclinic	Tetragonal	Orthorhombic
Space group	C2/m #12	P4/nmm #129	Imma #72
Pearson symbolmS8	tP4	oI8	oI8
Primitive vect.			
$\mathbf{a}_1/a$	(-1/2,1,-1/2)	(0,-1/2,-1/2)	(3/2,1/2,-1/2)
$\mathbf{a}_2/a$	(-1/2,1/2,-1)	(0,-1/2,1/2)	(1/2,3/2,1/2)
$\mathbf{a}_3/a$	(0,-2,2)	(-2,0,0)	(-1/2,-3/2,1/2)
Atomic Positions			
A1	(0,0,0)	(0,0,0)	(0,0,0)
A2	(0,0,3/4)	(1/2,1/2,3/2)	(1/4,3/4,1/2)
B1	(0,0,1/4)	(0,0,1/2)	(1/2,1/2,0)
B2	(0,0,1/2)	(1/2,1/2,1/4)	(3/4,1/4,1/2)
B3	—	—	—
B4	—	—	—
AFLOW label	“17”	“14”	“80”